



Holocene sea level and environmental change at the southern Cape - an 8.5 kyr multi-proxy paleoclimate record from lake Voëlvlei, South Africa

Paul Strobel¹, Marcel Bliedtner¹, Andrew S. Carr², Peter Frenzel³, Björn Klaes⁴, Gary Salazar⁵, Julian
5 Struck¹, Sönke Szidat⁵, Roland Zech¹, Torsten Haberzettl⁶

¹Physical Geography, Institute of Geography, Friedrich Schiller University Jena, Jena, Germany

²School of Geography, Geology and the Environment, University of Leicester, Leicester, UK

³Institute of Geosciences, Friedrich Schiller University Jena, Jena, Germany

⁴Department of Geology, University of Trier, Trier, Germany

10 ⁵Department of Chemistry and Biochemistry and Oeschger Centre for Climate Change Research, University of Bern, Bern, Switzerland

⁶Physical Geography, Institute of Geography and Geology, University of Greifswald, Greifswald, Germany

Correspondence to: Paul Strobel (paul.strobel@uni-jena.de)

Abstract.

15 South Africa is a key region for paleoclimate studies reconstructing and understanding past changes in atmospheric circulation, i.e., temperate Westerlies and tropical Easterlies. However, due to the scarcity of natural archives, the environmental evolution during the late Quaternary remains highly debated. Many archives that are available are peri-coastal lakes and wetlands and sea level changes during the Holocene often overprinted the paleoenvironmental signals in these archives. This study presents a new record from the coastal wetland Voëlvlei, which is an intermittent lake situated in the year-round rainfall zone (YRZ)
20 of South Africa at the southern Cape coast. It presents an ideal archive to investigate both sea level and environmental changes. A 13 m-long sediment core was retrieved from Voëlvlei and analysed using a multi-proxy approach. The chronology reveals a basal age of 8,440 ^{+200/-250} cal BP. Paleoecological and elemental analyses indicate marine intrusions from 8,440 to 7,000 cal BP with a salinity optimum at 7,030 ^{+150/-190} cal BP. Since 6,000 cal BP, silting up has been causing an intermittent freshwater lake.

25 Inferred from changes in allochthonous input, $\delta^{13}\text{C}_{n\text{-alkane}}$ and $\delta^2\text{H}_{n\text{-alkane}}$ increasing moisture is observed from 8,440 ^{+200/-250} cal BP. The $\delta^2\text{H}_{n\text{-alkane}}$ record provides new evidence in contribution of different precipitation sources throughout the record with contributions from both Westerlies and Easterlies from 8,440 to 7,070 cal BP. Westerlies dominate from 7,070 to 6,420 cal BP followed by a distinct shift to an Easterly-dominance at 6,420 cal BP. An overall trend to a Westerly- lasting until 2,060 cal BP is followed by a trend towards an Easterlies-dominance, but both phases show several climatic spikes. Those
30 spikes are also evident in other regional studies highlighting that the source and seasonality of precipitation has a mayor role for the hydrological balance. By comparing the Voëlvlei record with other regional studies, a similar trend in the overall moisture evolution along the southern Cape coast is inferred during the past 8.500 yrs.



1 Introduction

A record-breaking drought occurred in South Africa from 2015 to 2017 and future climate projections are even worse for large parts of the country (Engelbrecht and Engelbrecht, 2016; Engelbrecht et al., 2011). To make climate models and predictions of further hydrological change more reliable, robust paleoclimate reconstructions using direct hydrological proxies are necessary, which are hitherto very rare in South Africa (Haberzettl et al., 2014). Southern Africa's past and present climate has been driven by complex interactions between two major oceanic and atmospheric circulation systems, i.e., the Benguela and Agulhas current, and the Westerlies and Easterlies (Tyson and Preston-Whyte, 2000) (Fig. 1 A). Today, three major rainfall zones occur in South Africa. While the eastern and central parts of the country receive most rainfall (> 66%) from tropical moisture-bearing atmospheric circulation systems during austral summer (Summer Rainfall Zone, SRZ), a narrow belt along the west coast receives most rainfall (> 66%) from temperate Westerlies during the austral winter (Winter Rainfall Zone, WRZ) (Fig. 1 A). An intermediary area between the SRZ and WRZ receives rainfall from both systems throughout the year (Year-round Rainfall Zone, YRZ) (Fig. 1 A) (Engelbrecht et al., 2015; Scott and Lee-Thorp, 2004), and this includes the southern Cape coast, which is the focus of this study.

The YRZ has been the focus of most paleoenvironmental and associated -paleoclimatic research. There, the southern Cape coast and especially the Wilderness area with its numerous coastal lakes including such as Bo Langvlei (du Plessis et al., 2020), Eilandvlei (Kirsten et al., 2018a; Kirsten et al., 2018b; Quick et al., 2018; Reinwarth et al., 2013; Wündsche et al., 2018; Wündsche et al., 2016b), Groenvlei (Martin, 1959, 1968; Wündsche et al., 2016a) and Swartvlei (Birch et al., 1978; Haberzettl et al., 2019) has yielded multiple paleoenvironmental records (Fig. 1 B). These coastal lakes have formed between large coastal dune cordons that lie parallel to the coast. However, the terrestrial climate signals in these coastal archives are often overprinted by marine water intrusions induced by relative sea level change during the Holocene (Martin, 1959, 1968; Reinwarth et al., 2013; Wündsche et al., 2018; Wündsche et al., 2016a) or anthropogenic impact (Haberzettl et al., 2019). Further paleoenvironmental information from this area is available from e.g., peatlands (Quick et al., 2016; Strobel et al., 2019) and speleothems (Braun et al., 2018; Braun et al., 2020; Talma and Vogel, 1992), rock hyrax midden (Chase et al., 2019; Chase et al., 2020; Chase et al., 2017; Chase et al., 2018; Chase et al., 2015) and marine sediments (Hahn et al., 2017) (Fig. 1 A). However, the climate evolution of South Africa is still debated, reflecting potential spatial variability in climate drivers at the regional scale, and due to the application of different methodological approaches in various studies (Chase and Quick, 2018; Strobel et al., 2019). Consequently, the understanding of environmental dynamics and changing interactions between tropical and temperate climate systems affecting the YRZ is limited.

Compound-specific stable isotope analyses of hydrogen and carbon isotopes of long-chain *n*-alkanes ($\geq C_{25}$; $\delta^2H_{n\text{-alkane}}$, $\delta^{13}C_{n\text{-alkane}}$) are valuable proxies that complement established methodological approaches related to paleoenvironmental and paleohydrological changes in sediment archives, e.g., grain sizes, geochemistry and pollen. Long-chain *n*-alkanes are leaf waxes produced by higher terrestrial plants and serve as valuable biomarkers, as they remain well preserved in soils and sediments over millennia because of their low water solubility and high resistance against degradation (Eglinton and Eglinton,



2008; Sachse et al., 2012; Sessions, 2016). In South Africa, the $\delta^2\text{H}_{n\text{-alkane}}$ signal shows the potential to reconstruct the isotopic signal of precipitation and thus directly refers to the precipitation source (Herrmann et al., 2017; Strobel et al., 2020). Although, $\delta^2\text{H}_{n\text{-alkane}}$ has hitherto rarely been used in terrestrial archives at the southern Cape coast (Strobel et al., 2019).

70 $\delta^{13}\text{C}_{n\text{-alkane}}$ is a suitable proxy to infer past changes in the vegetation composition (e.g., Diefendorf and Freimuth, 2017) as well as variations in plant water use efficiency and thus drought stress (Diefendorf and Freimuth, 2017; Struck et al., 2020). Therefore, using the climatic information from both leaf wax isotopes enables climate reconstructions based on the isotopic signal of precipitation, which can reflect local water availability. Further, leaf wax-derived *n*-alkanes can be used as a chronological marker since they can be dated using ^{14}C analyses (Bliedtner et al., 2020; Bliedtner et al., 2018; Douglas et al., 2014; Gierga et al., 2016; Haas et al., 2017).

75

[Figure 1]

Here we present a sediment record from Voëlvlei, today an intermittent lake, to reconstruct past sea level and environmental changes at the southern Cape coast of South Africa. Therefore, a multi-proxy approach has been applied to the sediments 80 comprising compound-specific stable isotope analyses on leaf waxes as well as established sedimentological, and (in)organic elemental, and paleoecological analyses on fossil associations. Specifically we aim at:

- i) establishing a robust chronology based on diverse dating approaches on different sediment compounds,
- ii) disentangling marine and climate influences during the development of lake Voëlvlei, and
- iii) inferring variations in local moisture availability and the source of precipitation.

85 2 Site description

Voëlvlei is situated ca. 40 km east of Still Bay and 30 km west of Mossel Bay, at an elevation of 5 m above present sea level (a.s.l.) ~10 km inland of the Indian Ocean coast. Today, Voëlvlei has an area of 3.8 km² (max. length 4.2 km; max. width 0.7 km) (Database: SRTM 1 arc-second) and the catchment has an area of 165 km² (Database: SRTM 1 arc-second) (Fig. 1 C). The catchment comprises altitudes between 5 and 333 m a.s.l. (Database: SRTM 1 arc-second) and is drained by one main 90 ephemeral river, which enters Voëlvlei in the north. A barrier elevated up to 17 m a.s.l. (Database: SRTM 1 arc-second) defines the southern border of the Voëlvlei catchment. Voëlvlei has one intermittent outflow in the southwest at 6 m a.s.l. (SRTM 1 arc-second) and drains into the Gouritz river (Fig. 1 C).

The geology is characterised by Palaeozoic quartzites of the Table Mountain Group (Cape Supergroup), mudrock-sandstones of the Bokkeveld Group (Cape Supergroup), Mesozoic mudrock-sandstone conglomerates (Uitenhage Group), and 95 Cenozoic limestone-sandstone conglomerates (Bredasdorp Group) (Johnson et al., 2006). Soils have high aluminium and iron concentrations and are mostly Cambisols and Leptosols (Fey, 2010; Zech et al., 2014).



The potential natural vegetation consists of variations of Fynbos and only small areas along the main drainage system would be covered by Albany Thicket (Mucina and Rutherford, 2006). Today, large areas of the catchment are used for agriculture and some pastures persist. The steep slopes of the drainage system are mainly unmanaged and covered by plant communities of the Fynbos and Albany Thicket.

Mean annual precipitation at the study site is $450 \text{ mm} \cdot \text{a}^{-1}$ (Fick and Hijmans, 2017) and rainfall is almost equally distributed throughout the year. Winter precipitation is linked to the temperate Westerlies related to the Atlantic ocean as moisture source, and summer precipitation is associated with the tropical Easterlies and the Indian Ocean as moisture source (Engelbrecht and Landman, 2016). Moreover, orographic rainfall occurs from local sources due to onshore flows related to ridging anticyclones (Weldon and Reason, 2014). The isotopic composition of precipitation ($\delta^2\text{H}_p$) is ^2H depleted during winter and ^2H enriched during summer periods, with a modelled annual mean of $-13 \pm 1 \text{ ‰}$ (Table 1) (Bowen, 2018; Bowen et al., 2005; Braun et al., 2017; Harris et al., 2010). Mean annual temperature is 17.6 °C and slightly higher temperatures during summer (22 °C) lead to semi-arid climatic conditions at the study site today (Fick and Hijmans, 2017).

[Table 1]

3 Material and Methods

For this study, the 13 m long sediment core VOV16 was retrieved from Voëlvlei (34.259°S ; 21.826°E) (Fig. 1 C) in 2016 using a motor hammer coring system (inner core diameter 5 cm) and transported to the Physical Geography laboratory of the Friedrich Schiller University Jena where it was stored dark and cool at $+4^\circ\text{C}$ until processing. Cores were split, photo- documented and described in detail concerning sedimentological properties and sediment colour in the laboratory.

3.1 Chronology

3.1.1 Radiocarbon dating of macro particle, bulk TOC and n-alkane samples

The chronology of the sediment record is based on ^{14}C -ages from one organic macro particle, three charcoal samples, 15 bulk organic samples and seven *n*-alkane samples (compound-class). 12 of the bulk organic samples and the organic macro particle were analysed with the AMS at the Poznan Radiocarbon Laboratory, Poland. Three bulk organic, three charcoal and seven *n*-alkane samples (cf., section 3.7 for sample extraction prior to measurement) were analysed with the Mini Carbon Dating System (MICADAS) AMS coupled to an element analyser (Ruff et al., 2010; Salazar et al., 2015; Szidat et al., 2014) at the LARA AMS Laboratory, University of Bern, Switzerland. ^{14}C results from the LARA AMS were reported as F^{14}C and corrected for cross and constant contamination after Salazar et al. (2015).



125 3.1.2 OSL dating

A split (half) section of the core was sub-sampled under red light conditions in the University of Leicester luminescence dating laboratory. The upper 5-6 mm of the sediment surface was removed, and the core section was sampled over a depth range of 70 mm. Sediment within 6-7 mm of the core tube inner surface was not sampled but was used for an estimation of sample water content. This (dry) material, as well as material from the upper surface was homogenised and used for dose rate analysis.

130 The sediment taken for equivalent dose analysis was soaked in sodium hexametaphosphate and then wet sieved. The core sediments yielded relatively limited amounts of sand sized material, most of which fell within the fine sand range ($< 100 \mu\text{m}$). This necessitated the use of the fine sand range 55-90 μm for equivalent dose analysis. This material was then prepared using standard methods. This involved treatment with dilute (10%) hydrochloric acid and (32%) hydrogen peroxide. The sample was then dried, and density separated to isolate the $< 2.7 \text{ g}\cdot\text{cm}^{-3}$ and $> 2.58 \text{ g}\cdot\text{cm}^{-3}$ fraction, before etching for 45 minutes in 48%
135 hydrofluoric acid, washing in hydrochloric acid and dry sieving.

Dose rates were determined using the remaining core material via inductively coupled plasma mass spectrometry (ICP-MS) for U and Th and ICP-OES for K analyses at the University of Leicester. The concentrations of U, Th and K were converted to annual dose rates following Guérin et al. (2011) with corrections for grain size (Mejdahl, 1979), water content (Aitken, 1985) and HF etching (Bell, 1979). Cosmic dose rates were determined using the reported sample depth following Prescott
140 and Hutton (1994) with a 5% relative uncertainty included. Final age uncertainties incorporate 3% relative uncertainties for the dose rate conversion factors, grain size attenuation factor, water attenuation and HF etching, propagated via standard methods. HF etching is assumed to have entirely removed the α -irradiated outer portion of the quartz grains. It was assumed that the as-measured water content was appropriate, with a 3% (absolute content) uncertainty propagated to the final dose rate uncertainty.

145 All luminescence measurements were performed on a Risø DA20 TL/OSL reader. Stimulation (40 s at 125°C) was provided by blue LEDs (stimulation wavelength 470 nm) with OSL signals detected with an EMI 9235QA photomultiplier tube via a U-340 detection filter. Laboratory irradiations were delivered by a ^{90}Sr beta source with a dose rate (at the time of measurement) $\sim 7.58 \text{ Gy}\cdot\text{min}^{-1}$. Sample equivalent doses (D_e) were determined using the Single Aliquot Regeneration (SAR) protocol (Murray and Wintle, 2000, 2003; Wintle and Murray, 2006). All single aliquot measurements were carried out on
150 small (1 to 2 mm) aliquots, which given the grain size fraction analysed means there are likely more than 1000 grains per aliquot (e.g., Duller, 2008).

A dose recovery preheat experiment was used to assess the suitability of the SAR protocol in general, and the most appropriate preheating conditions. The overall dose recovery ratio across all preheating temperatures 160-260 °C was 0.97 ± 0.03 ($n=22$; zero overdispersion), with a ratio of 1.00 ± 0.02 ($n=3$) for the chosen preheat temperature combination of 240°C for ten seconds
155 (natural regeneration points) and a 220 °C cut heat for the test dose measurements. All SAR analyses comprised a 7-regeneration point sequence, which included a repeated (recycling) regeneration dose point, and IR depletion regeneration dose point to check for K feldspar contamination (Duller, 2003) and a zero-dose point. The 4 (unique) point dose response



160 curve was generated using the initial 0.64 seconds of stimulation, with a background signal from the last 8 seconds. Analyses were carried out in the “Analyst” software. Dose response curves were fitted with saturating exponential fits with D_e uncertainties incorporating counting statistics, curve fitting uncertainties and a 1% systematic uncertainty (Duller, 2007) (all calculated within the Risø Analyst software). The uncertainty in final D_e estimate also incorporates an additional beta source calibration uncertainty (3%).

3.1.3 Age modelling

165 For the final age-depth modelling, all aforementioned results were used. Bulk organic and *n*-alkane ^{14}C -ages from the terrestrial part of the sediment core were calibrated with the SHCal20 data calibration curve (Hogg et al., 2020), whereas ^{14}C -ages from the marine part of the record were calibrated with the Marine20 calibration curve (Heaton et al., 2020) and additionally corrected for a marine reservoir effect using a ΔR of 134 ± 38 ^{14}C yrs as previously reported by Wündsche et al. (2016b) (Table 1). For the compound-class *n*-alkane samples, the SHCal20 calibration curve (Hogg et al., 2020) was applied due to a predominance of terrestrial synthesized long-chain *n*-alkanes (C_{29} , C_{31} , C_{33}) in the samples (cf., section 4.3; Table 1). The 170 terrestrial organic macro particle and charcoal found in the marine part of the record were calibrated with the SHCal20 curve (Hogg et al., 2020) (Table 1). All calibrations were done with the online version of the Calib 8.2 software (Stuiver et al., 2020). The final age-depth relation was calculated with the R software package Bacon 2.4.3 (Blaauw and Christen, 2011), using the same calibration data sets.

3.2 Grain size analyses

175 For grain size measurement 50 mg sample aliquots were treated with H_2O_2 (10% p.A.) to remove organic matter, HCl (10% p.A.) for the destruction of carbonates, and $\text{Na}_4\text{P}_2\text{O}_7/\text{Na}_2\text{CO}_3$ for dispersion. The grain-size distribution of each sample was determined with a Laser Particle Sizer (FRITSCH ANALYSETTE 22 Microtec, FRITSCH, Germany) and a wet dispersion unit at the Physical Geography laboratory of the University of Greifswald. Before the measurement, samples were treated with ultrasound for 60 seconds and subsequently measured in duplicate. The grain size distribution is calculated in 99 classes 180 between 0.08 – 2,000 μm . The mean and median grain size as well as fractions of clay, silt and sand of each sample were calculated.

3.3 Paleontological analyses

185 A selection of 23 sediment samples representing all lithological units and focusing on the assumed transition from an estuarine to a freshwater environment was processed and analysed micropaleontologically. About 3-7 ml sediment from 1-cm thick sediment slices of the core were washed with tap water through stacked sieves of 63 μm and 200 μm mesh size. After drying the sieve residues on a heating plate at $\sim 50^\circ\text{C}$, all microfossils were picked under a low-power stereomicroscope and transferred to microfossil slides for later identification and counting. Microfossils, fragments of macrofossils and charcoal were documented semi-quantitatively as rare (1-2 specimens), common (>2), abundant (>10) and very abundant (>100).



190 Identification relies on Benson and Maddocks (1964), Martens et al. (1996) Fürstenberg et al. (2017) for Ostracoda and on
Schmitt-Sinns (2008) and Fürstenberg et al. (2017) for Foraminifera. Additionally, macrofossils found during the lithological
description, sampling of the core and processing the microfossils were identified, counted and used for paleoecological
interpretation. Those macrofossils are all snails identified relying mainly on Branch et al. (2010) and the mollusc section of
the World Register of Marine Species (www.marinespecies.org). Bivalves could not be identified because they occurred only
as fragments. Paleoecological information was drawn from the papers listed above for identification plus Murray (2006) and
195 Kirsten et al. (2018a). All paleontological material is stored in the collection of the authors at Friedrich Schiller University
Jena and will be transferred to the South African Museum of Natural History in Cape Town later.

3.4 Elemental analyses

XRF data were collected every 1 cm down-core using two generator settings (30 kV, 1 mA, 15 s; 15 kV, 0.2 mA, 15 s) for
detection of different elemental groups with XRF Core Scanner II (AVAATECH Serial No. 2) at MARUM - University of
200 Bremen. The split core surface was covered with a 4 micron thin SPEXCerti Prep Ultralene1 foil to avoid contamination of
the XRF measurement unit and desiccation of the sediment. The here reported data have been acquired by a Canberra X-PIPS
Silicon Drift Detector (SDD; Model SXD 15C-150-500) with 150eV X-ray resolution, the Canberra Digital Spectrum Analyzer
DAS 1000, and an Oxford Instruments 50W XTF5011 X-Ray tube with rhodium (Rh) target material. Raw data spectra were
processed by the analysis of X-ray spectra by Iterative Least square software (WIN AXIL) package from Canberra Eurisys.
205 Presented data were normalised by elemental Zr counts and plotted as log-ratios, primarily to eliminate sediment matrix errors
(water content, surface roughness and grain size variations) (Weltje and Tjallingii, 2008).

Moreover, 150 sample aliquots in an interval of 8 cm were freeze dried (-53 °C, for > 48 h), ground and sieved to a size
< 40 µm. Aluminium (Al), calcium (Ca) and sodium (Na) concentrations were measured with an ICP-OES 725-ES (VARIAN,
USA) at the Physical Geography laboratory of the Friedrich Schiller University Jena. 0.2 g of the samples was processed using
210 a microwave-assisted modified aqua regia digestion of 2 ml HCL (32% p.A.) and 4 ml HNO₃ (65% p.A.). Error estimates were
based on triple measurements of three samples (VOV_243, VOV_651, VOV_1186; numbers indicate sample depth) (relative
error: Al 3.7%; Ca: 5.4%; Na: 5.3%). Samples of the reference material LGC6 187 (river sediment) were measured as well to
calculate the relative analytical error which was 1.1% for Al and Ca, and 10% for Na.

Total nitrogen (TN) and total carbon (TC) were analysed with a CNS analyser (EuroVector EA 3000, HEKAtech GmbH,
215 Germany) at the Physical Geography laboratory of the University of Greifswald. Concentrations of total organic carbon (TOC)
were determined with the same device after treatment with 3% and 20% HCl at 80 °C to remove carbonates. Error estimates
were based on triple measurements of 30 samples (mean relative error: N: 8.9%; TOC: 2.9%). Total inorganic carbon (TIC)
was calculated as difference between TC and TOC.



3.5 Biogenic Silica (BiSi)

220 Biogenic silica (BiSi) concentrations were determined following Ohlendorf and Sturm (2008). BiSi and Al concentrations were measured using an ICP-OES 725-ES (VARIAN, USA) at the Physical Geography laboratory of the Friedrich Schiller University Jena. A correction factor of one (BiSi:Al; 1:1) was applied to account for dissolving aluminosilicates.

3.6 Powder X-ray diffraction (XRD)

225 The identification of the mineral composition of 50 powdered samples (e.g., Pecharsky and Zavalij, 2009) from representative sediment core sections was carried out using an X-ray diffractometer (D8-Discover, Bruker AXS) equipped with a CuK α X-ray tube and a gas proportional counter (HI-STAR area detector, Bruker AXS) at Friedrich Schiller University Jena. The qualitative analyses and interpretation of the diffractograms was conducted at Trier University using Bruker DIFFRAC plus 5.0 software. The occurrence of specific mineral phases (low, medium, high) was roughly estimated based on XRD peak intensities in conjunction with the elaborated geochemistry of the investigated sediment sections. For all measurements the
230 quartz peak at 3.342 Å was accepted as internal standard.

3.7 Biomarker analyses of *n*-alkane distributions and stable isotope compositions

Total lipids of the sediment samples (14.5 – 31.4 g) were extracted with 40 ml dichloromethane (DCM) and methanol (MeOH) (9/1, v/v) using an ultrasonic bath over three 15 min cycles. The total lipid extract was separated by solid phase extraction using aminopropyl silica gel (Supelco, 45 μ m) as stationary phase. The *n*-alkanes were eluted with 4 ml hexane and further
235 purified over coupled silvernitrate (AgNO₃) – zeolite (Geokleen) pipette columns. The *n*-alkanes trapped in the zeolite were subsequently dissolved in hydrofluoric acid and recovered by liquid-liquid extraction using *n*-hexane. An Agilent 7890 gas chromatograph equipped with an Agilent HP5MS column (30 m, 320 μ m, 0.25 μ m film thickness) and a flame ionization detector (GC-FID) was used for identification and quantification of the *n*-alkanes, relative to external *n*-alkane standards (*n*-alkane mix *n*-C₂₁ - *n*-C₄₀, Supelco).

240 *n*-Alkane concentrations were calculated as the sum of C₂₅ to C₃₅, and are given in μ g · g⁻¹ dry weight. Odd-over-even predominance (OEP) values (eq. 1) were determined following Hoefs et al. (2002). Low values (<5) indicate an enhanced state of degradation (Buggle et al., 2010; Zech et al., 2010). The Average Chain Length (ACL) (eq. 2) was calculated from the odd-numbered *n*-alkanes (Poynter et al., 1989).

$$245 \quad \text{OEP} = \frac{(nC_{27} + nC_{29} + nC_{31} + nC_{33})}{(nC_{26} + nC_{28} + nC_{30} + nC_{32})} \quad (\text{eq. 1})$$

$$\text{ACL} = \frac{27 \cdot nC_{27} + 29 \cdot nC_{29} + 31 \cdot nC_{31} + 33 \cdot nC_{33}}{nC_{27} + nC_{29} + nC_{31} + nC_{33}} \quad (\text{eq. 2})$$



Compound-specific stable hydrogen isotope analyses of the C₃₁ and C₃₃ *n*-alkanes were carried out on an IsoPrime 100 IRMS,
250 coupled to an Agilent 7890A GC via a GC5 pyrolysis or combustion interface operating in pyrolysis modus with a MaxChrome
and silver wool packed reactor at 1050 °C. Samples were injected with a split–splitless injector. The GC was equipped with
30 m fused silica column (HP5-MS, 0.32 mm, 0.25 µm). Each sample was analysed in triplicate, except for single
measurements of three samples (VOV_915, VOV_128, VOV_111; numbers indicate sediment depth) due to insufficient
compound abundance. δ²H_{*n*-alkane} was measured against calibrated H₂ reference gas and all values are reported in ‰ against
255 VSMOW. The precision was checked by co-analysing a standard alkane mixture (*n*-C₂₇, *n*-C₂₉, *n*-C₃₃) with known isotope
composition (Arndt Schimmelmann, University of Indiana), injected in duplicate every nine runs. All measurements were
corrected for drift and amount dependency, relative to the standard values in each sequence. Triplicates for the C₃₁ and C₃₃
alkanes had a standard deviation of <4.0 ‰, the analytical error for the standards was <1.7 ‰ (*n* = 68). The H₃⁺ factor was
checked every two days and stayed stable at 4.40 ± 0.03 during measurements.

260 Compound-specific stable carbon isotope analyses of C₃₁ and C₃₃ *n*-alkanes were carried out on an IsoPrime 100 IRMS,
coupled to an Agilent 7890A GC via a GC5 pyrolysis or combustion interface operating in combustion modus with a CuO and
silver wool packed reactor at 850 °C. Samples were injected with a split–splitless injector. The GC was equipped with 30 m
fused silica column (HP5-MS, 0.32 mm, 0.25 µm). δ¹³C_{*n*-alkane} values were calibrated against CO₂ reference gas of known
isotopic composition and all carbon isotope values are given in ‰ against VPDB. Triplicate injections were conducted for
265 each sample and measurement accuracy was controlled in the same way as for the δ²H_{*n*-alkane} analyses. Triplicates for the C₃₁
and C₃₃ alkanes had a standard deviation of <0.2 ‰, the analytical error for the standards was <0.2 ‰ (*n* = 83).

4 Results

4.1 Lithology and Chronology

The sediment sequence has a length of 13 m and consists of three lithological units based on differences in sediment colour
270 (Fig. 2). Unit A from 13 to 4.51 m sediment depth consists of dark greyish material and is dominated by silt. Within this unit,
several thin greyish clayey and yellowish sandy layers are present. Unit B from 4.51 to 0.78 m sediment depth consists of
brownish to reddish silty material. In the lower parts of Unit B thin greyish clayey layers are observed. Unit C from 0.78 m
sediment depth to the top is dominated by dark brown silty material. Moreover, two layers (0.53 - 0.44; 0.31 - 0 m sediment
depth) can be separated through changes in colour and granulometric structure in Unit C (Fig. 2).

275

[Figure 2]

The chronology of the sediment record reveals a basal age of 8,440 ⁺²⁰⁰/₋₂₅₀ cal BP (Fig. 2, Tab 2). In Unit A, ¹⁴C-ages of the
bulk samples are stratigraphically consistent, except for two samples at 11.19 and 5.66 m sediment depth, which are too young
280 for their stratigraphic position. The ¹⁴C-age ranges of a terrestrial organic macro particle and a reservoir corrected bulk



sediment sample at 9.63 and 9.61 m overlap. At 4.57 m sediment depth, two charcoal samples and a reservoir corrected bulk sediment sample distinctly overlap as well. Above the bulk sediment sample at 4.57 m sediment depth, four bulk sediment samples are too old for their stratigraphic position and amongst them not in stratigraphic order (Unit B and C). In contrast, ^{14}C -ages of compound-class *n*-alkane samples are distinctly younger and in stratigraphic order in Unit B and C (Tab 2; Fig. 2).

285 Consistent with the good dose recovery results the OSL sample produced a bright, rapidly decaying quartz OSL signal (reduced to ~2% of the initial signal within 1 second). None of the analysed aliquots exhibited recycling ratios or IR ratios beyond / below (respectively) 10% of unity or recuperation (zero dose signal) > 1% of the natural signal. The equivalent dose distribution however is overdispersed ($40 \pm 5\%$; Table 3), even after removal of one very high (125 Gy) outlier, despite the

290 considerable signal averaging likely associated with the use of the fine sand fraction for analysis. In the context of the analysed core, its likely antiquity, and the otherwise excellent performance of the sample implied by the dose recovery experiment and internal checks with in the SAR protocol, a parsimonious explanation of this broad distribution is the presence of unbleached or incompletely bleached grains. Indeed, the age obtained from the central age model equivalent dose estimate is 10 ± 1 ka, which is implausible given the stratigraphic position of the sample (Fig. 2). Application of a 3-component minimum age model (Galbraith et al., 1999) administered in the R package “Luminescence” (Burrow, 2019) produces a D_e estimate of 20.3 ± 2.4

295 Gy and an age of 6.8 ± 0.8 ka (Table 3). While caution is required when applying this approach to multi-grain aliquots (especially those with considerable signal averaging as here), the minimum age estimate is much more concordant with the radiocarbon ages from this section of the core, and the broader age-depth model for the whole sequence (Fig. 2). In addition to that the MAM OSL-age is in stratigraphic order with the ^{14}C -ages of compound-class *n*-alkane and charcoal samples (Fig. 2).

300 [Table 2]

[Table 3]

4.2 Geochemical and paleontological analyses

Significant correlations (Pearson’s r ; $\alpha < 0.05$) were obtained for the log-normalised XRF scanning data for Br/Zr and Al/Zr compared to the quantitative elemental contents of Na and Al, respectively (r : $\text{Log}(\text{Br/Zr}) / \text{Na} = 0.82$; r $\text{Log}(\text{Al/Zr}) / \text{Al} =$

305 0.71 ; Fig. 3). Na concentrations range from $2,090 \pm 110$ to $10,390 \pm 550$ ppm over the sequence. Both Na contents and Br/Zr-ratios show highest values in Unit A (13 - 4.51 m sediment depth). Several minima in the Br/Zr-ratios derived from XRF-scanning data are not visible in the Na concentrations due to the higher sample resolution of the XRF-data (Fig. 3). Both Na concentration and Br/Zr-ratios distinctly decrease above 4.51 m sediment depth, but an increase is noticeable in Unit C (<0.78 m sediment depth) (Fig. 3). Al concentrations range from $39,300 \pm 1,500$ to $82,900 \pm 3,100$ ppm, and both Al contents

310 and Al/Zr-ratios show high values over large parts of the sediment record. As aforementioned, Al/Zr-ratios show minima in Unit A, which are not visible in the Al concentrations due to the higher sample resolution of the XRF-scanning data (Fig. 3). Noticeable are distinct low values of Al concentrations and Al/Zr-ratios from 4.51 to 2.91 m sediment depth and at 1.82 m sediment depth with an increasing trend to the top of the record (Fig. 3). TOC and N range from 0.16 to 3.94% and 0.03 to



0.48% respectively and show high values in the lower parts, strongly reduction above 4.51 m sediment depth and increase
315 thereafter again (Fig. 3). The C/N molar ratio ranges between 1.9 and 13.6 over the whole sequence with high values between
5.15 and 4.27 m sediment depth (Fig. 3). TIC ranges from 0 to 0.86% with noticeable peaks between 6.91 and 6.51, and at
4.83, 2.59 and 1.74 m sediment depth (Fig. 3). Ca contents show a similar pattern like TIC and ranges from $2,830 \pm 150$ to
 $28,900 \pm 1,600$ ppm (Fig. 3). BiSi concentrations range from 0.8 ± 0.02 to $2.8 \pm 0.08\%$ with low values in the lower parts of
the record (>6.99 m sediment depth), except for high values between 10.98 and 10.10 m sediment depth
320 ($1.6 \pm 0.05 - 2.2 \pm 0.07\%$)(Fig. 3). They show high values for the upper part of the record <6.91 m sediment depth (Fig. 3).
Apart from the selected mineral components of the XRD measurements displayed in Fig. 3, all samples have a predominance
of quartz, feldspars and micas. Calcite follows the patterns of TIC and Ca and shows highest abundances between 11.46 and
10.18 as well as 3.87 and 2.19 m sediment depth (Fig. 3). The other sections have only medium to low proportions of calcite
(Fig. 3). The presence of gypsum is restricted to depths between 9.62 and 9.14 m as well as 5.47 and 5.23 m (Fig. 3). However,
325 an absence of calcite and/or gypsum at the distinct peaks of TIC and Ca (e.g., 1.74 and 2.59 m sediment depth) is likely due to
the lower sample resolution of the XRD measurements compared to the elemental data (Fig. 3). High proportions of halite are
present in large parts of the sediment record (>2.19 m sediment depth; Fig. 3).

[Figure 3]

330

n-Alkane concentrations range from 0.22 to 5.23 $\mu\text{g}\cdot\text{g}^{-1}$ with high values in Unit A and distinctly lower concentrations in Unit
B and C (Fig. 4). All samples show a distinct odd over even predominance (4.0 - 15.5) and the ACL ranges from 29.9 to 31.4.
Consequently, C_{29} , C_{31} and C_{33} are the predominant *n*-alkane chain-lengths in all samples (Fig. 4). $\delta^{13}\text{C}_{n\text{-alkane}}$ values range
from -28.10 ± 0.16 to $-22.72 \pm 0.06\%$ with ^{13}C depleted values at the bottom of Unit A, followed by more ^{13}C enriched
335 $\delta^{13}\text{C}_{n\text{-alkane}}$ values, which show a decreasing trend upwards (Fig. 4). Remarkable are three strongly ^{13}C enriched $\delta^{13}\text{C}_{n\text{-alkane}}$
values in the upper parts of Unit A between 6.35 and 4.51 m sediment depth (Fig. 4). $\delta^2\text{H}_{n\text{-alkane}}$ values range from -154.4 ± 1.3
to $-129.6 \pm 1.1 \%$ with ^2H enriched values at the bottom followed by a trend to ^2H depleted values in Unit A. Unit B shows ^2H
enriched values at the bottom followed by ^2H depleted values at the top and in Unit C (Fig. 4).

340 [Figure 4]

Paleontological analyses of the 33 macrofossil samples plus 23 microfossil samples revealed 56 snail specimens representing
six species. In descending order of abundance these are *Turritella capensis* (Krauss, 1848), which is clearly dominant, the rare
Assiminea globulus (Conolly, 1939), *Hydrobia* sp., *Natica tecta* (Anton, 1839), *Nassarius kraussianus* (Dunker, 1846) and a
345 fragment of an unidentified gastropod species (Fig. 5). The microfossil associations show a higher diversity (Fig. 5). The
dominating foraminifer taxon is *Ammonia parkinsoniana* (d'Orbigny, 1839), followed by *Quinqueloculina* sp., and the rare
Trochammina inflata (Montagu, 1808) and *Haynesina* sp. All other foraminifer taxa are represented by only one test each



(*Bolivina* sp., *Criboelphidium articulatum* (d'Orbigny, 1839), *Spirillina* sp. and an unidentified trochamminid). The most abundant ostracod species are *Sulcostocythere knysnaensis* Benson and Maddocks, 1964 and juveniles of *Loxoconcha*
350 *parameridionalis*? Benson and Maddocks, 1964, rare ostracods are a myodocopid specimen and juvenile *Aglaiella* valves as well as the freshwater species *Sarscypridopsis aculeata* (Costa, 1847), *Cyprilla humilis* Sars, 1924 and an unidentifiable fragment of a larger species (Fig. 5). Microfossils identified on a group level only are ehippia of cladocerans, gyrogonites of charophytes, *Plumatella*-like bryozoan statoblasts, mollusc and insect fragments, fish bone remains, fruits and seeds as well as unidentifiable plant remains. Charcoal was found in large quantities in many samples.

355 Unit A1 shows a high diversity and contains most of the marine-brackish snails and high numbers of foraminifers (Fig. 5). The ostracod fauna is dominated by brackish water taxa. Shell and fish bone fragments are abundant. Unit A2 looks similar as Unit A1 but is generally more variable in abundances and diversity. Macrofossils, i.e., marine-brackish snails, become rare. Saltmarsh foraminifers, fruits and seeds occur for the first time (Fig. 5). Units B and C lack marine-brackish snails, brackish ostracods and saltmarsh foraminifers, and foraminifers in general are documented with a single test at the base of the zone
360 only. Freshwater ostracods occur for the first time and freshwater taxa in general dominate. Fragments of shells, plants, insects and charcoal disappear in Unit B and C (Fig. 5).

[Figure 5]

5 Discussion

365 5.1 Chronostratigraphy

Micropaleontological and (in)organic analyses show that three different depositional settings exist for the sediment sequence from Voëlvei (Fig. 3, 5). In the lower part of the sequence (Unit A), the high concentrations of Na, TOC and N, high Br/Zr-ratios and marine/brackish gastropod species indicate a marine/brackish depositional setting from 13 to 4.51 m sediment depth (Fig. 2, 3, 5). Corresponding reservoir corrected bulk sediment, a terrestrial organic macro-particle and charcoal ¹⁴C-ages are
370 stratigraphically consistent and range from 8,510^{+280/-200} to 6,310^{+450/-210} cal BP indicating that sediments were rapidly deposited (Fig. 2). The distinct overlap of a bulk and the macro-particle age and bulk and charcoal ages confirm the reservoir correction and application of the Marine20 calibration curve (Heaton et al., 2020) for bulk samples in Unit A. The only exception are the bulk ¹⁴C-ages at 11.19 and 5.66 m sediment depth, which are too young for their stratigraphic position. This is probably due to an increased input of terrestrial organic carbon during this time indicated by high input of sand and reduced
375 Al contents and Al/Zr-ratios (Fig. 2, 3) which likely adds less ¹⁴C depleted material affecting the marine organic carbon stock and diluting the reservoir effect. As we cannot calculate the precise contribution of terrestrial organic carbon, these ¹⁴C-ages were excluded from the age model in a second modelling iteration (Heaton et al., 2020; Hogg et al., 2020) (Fig. 2).

At Voëlvei, *n*-alkanes show a clear dominance of the longer chains C₃₁ and C₃₃, and thus are of terrestrial origin (Boom et al., 2014; Chambers et al., 2014; Strobel et al., 2020). Therefore, we calibrated them with the terrestrial SHCal20 calibration curve.



380 We note that minor contribution of the shorter chains ($<C_{25}$) to the dated compound-class *n*-alkane samples, which are synthesised by e.g., aquatic plants and possibly show a marine reservoir effect, would lead to too old ^{14}C -ages when calibrated using SHCal20 calibration curve. The aforementioned dominance of long-chain *n*-alkanes however makes a terrestrial origin likely and the distinct overlap with marine calibrated and reservoir corrected bulk ^{14}C -ages support the application of the SHCal20 calibration curve to the compound-class *n*-alkane samples (Fig. 2).

385 At 4.51 m sediment depth, a distinct shift in the depositional setting occurred with decreasing Na concentrations, Br/Zr-ratios, and TOC and N concentrations, pointing towards a change of the marine/brackish to a lacustrine environmental setting (Fig. 3, 5). Bulk ^{14}C -ages are much older than their stratigraphic position and possibly show the deposition of degraded pre-aged sediments, possibly due to erosion of old organic carbon from deeper soil horizons within the catchment (Bliedtner et al., 2020; Douglas et al., 2018; Haas et al., 2020). The OSL-age is stratigraphically more consistent than the bulk ^{14}C -ages. Since a MAM

390 was applied it is likely that this age reflects the timing of deposition, but the presence of a tailing of partially or unbleached sand grains also potentially implies an input from older sediments at this time, supporting the interpretation of the bulk ^{14}C -age over-estimations. Compound-class *n*-alkane ^{14}C -ages are stratigraphically consistent in Unit B and C. We therefore infer that leaf waxes derived from topsoils in the catchment and are rapidly deposited in the sediment archive (Bliedtner et al., 2020; Haas et al., 2017). Therefore, the incorporated climate signal should be close to that of the timing of deposition and *n*-alkane-

395 based proxies, i.e., $\delta^{13}C_{n\text{-alkane}}$ and $\delta^{13}C_{n\text{-alkane}}$, yield paleoenvironmental information that can also be interpreted robustly.

5.2 Marine influence and lake development

South Africa, especially the southern Cape coast, is known to have experienced distinct environmental changes related to relative sea level fluctuations during the Holocene (Cooper et al., 2018; Kirsten et al., 2018b; Wündsche et al., 2018; Wündsche et al., 2016a). Voëlvlei provides the possibility to contribute to our understanding of sea level changes during the Holocene

400 due to its present location at an elevation of 5 m a.s.l. and the high temporal resolution in the Early and Mid-Holocene. Inferred from lithological characteristics, paleoecological and elemental analyses, which indicate variable intrusion of marine waters, the record provides three eco-zones of which one can be subdivided in two subzones (Unit A1, A2, and B and C) (Fig. 6). During the period between 8,440 $^{+200}/_{-250}$ and 7,070 $^{+160}/_{-200}$ cal BP (Unit A1), the dominant gastropod *Turritella capensis* is a common modern species in sand in South African lagoons (Branch et al., 2010) preferring the mid-intertidal zone (Walters and Griffiths, 1987) (Fig. 5, 6). The rarer gastropod *Assiminea globulus* is known to be very abundant on upper intertidal mudflats of South African estuaries today (Barnes, 2018), whereas the small gastropod *Hydrobia* prefers the upper salt marshes of South Africa (Branch et al., 2010). The single occurrences of *Natica tecta* and *Nassarius kraussianus* point to estuarine mudflats (Branch et al., 2010) (Fig. 5, 6). Abundant brackish water ostracods and foraminifers indicate permanent water cover at the coring site in this period. Summarising, the fauna reflects an estuarine and shallow subtidal environment close to

410 intertidal mudflats. The abundance of plant remains and fragments of shells and fish bones point to shallow water as well. Therefore, we assume the respective core depths reflect an elevation slightly below the past sea level, which is in line with the paleo-surface of lake Voëlvlei, i.e., 8.0 to 3.5 m below present sea level (b.s.l.) from 8,440 $^{+200}/_{-250}$ to 7,070 $^{+160}/_{-200}$ cal BP



(Fig. 6). The low diversity of foraminifers is typical for lower salinity conditions, the dominant small and unornamented *Ammonia* species, *Quinqueloculina* and *Haynesina* are consistent with this brackish water inference (Murray, 2006) (Fig. 5, 415 6). The same applies to the brackish water ostracod fauna, which are dominated by the estuarine species *Sulcostocythere knysnaensis* and *Loxococoncha parameridionalis* (Fürstenberg et al., 2017; Kirsten et al., 2018a) (Fig. 5, 6). The complete absence of open marine microfossils, especially planktic foraminifers and echinoderm fragments, indicates an inner estuarine position in the core locality without direct marine inflow, even under high-energy conditions. The few bryozoan statoblasts and gyrogonites of charophytes all derive from freshwater environments (Frenzel, 2019; Kirsten et al., 2018a) and point to an 420 unconfined exchange with river water. The highest salinity for the entire core is probably reached at 7,090 ⁺¹⁷⁰/₋₂₀₀ cal BP when foraminifer abundance and diversity reach a maximum and a myodocopid ostracod was found (Fig. 5, 6). The coring position was ~3.65 m b.s.l. during this time (Fig. 6). Therefore, sea level was likely at the present height or slightly lower.

Between 7,070 ⁺¹⁷⁰/₋₂₀₀ and 6,420 ⁺¹³⁰/₋₁₄₀ cal BP (Unit A2), continued inner estuarine, brackish water conditions are indicated by a similar assemblage of taxa as observed in Unit A1. Intertidal gastropods typical for Unit A1, however, are now very rare, 425 suggesting decreasing tidal influence and probably decreasing salinity (Fig. 5, 6). Salt marsh foraminifers occur only in Unit A2, albeit in low numbers (Fig. 6). This points to a very shallow water depth under marine/brackish conditions and a close shoreline (Strachan et al., 2017), which is in good agreement with the occurrence of fruits and seeds, only occurring in this unit, and abundant plant remains. However, the high variability in the abundance of many taxa indicates unstable conditions compared to Unit A1. Freshwater inflow is implied by floating bryozoan statoblasts and charophyte gyrogonites (Frenzel, 430 2019) (Fig. 5, 6). The respective paleo-surface of lake Voëlvlei was ~3.5 m b.s.l. to 0.5 m a.s.l. from 7,070 ⁺¹⁷⁰/₋₂₀₀ to 6,420 ⁺¹³⁰/₋₁₄₀ cal BP (Fig. 6) indicating a sea level higher than the present during this time.

Elemental (Br/Zr-ratios, Na contents) and mineralogical data support phases of marine water intrusions at lake Voëlvlei. Bromide salts are common in sea water, but occur in very low concentrations in freshwater systems (Song and Müller, 1993). In aqueous environments the dominant species is Br⁻, which substitutes the salt constituent chloride (Cl⁻) in the sea salt lattice 435 during crystallization (Ullman, 1995). Halite (NaCl) also originates from marine waters, and thus Br, Na and halite can be used as indicators of marine water intrusion (Babel and Schreiber, 2014; Olsen et al., 2012; Wüdsch et al., 2018). High values of the marine indicators from the elemental analysis (Na, Br/Zr-ratios) and the presence of halite in the sediments are in good agreement with our micropaleontological data indicating marine water intrusions in Units A1 and A2 (8,440 ⁺²⁰⁰/₋₂₅₀ to 6,420 ⁺¹³⁰/₋₁₄₀ cal BP; Fig. 6). Furthermore, the occurrence of calcite in both units, as well as gypsum from 7,260 ⁺¹¹⁰/₋₂₁₀ to 440 7,180 ⁺¹⁵⁰/₋₂₀₀ cal BP and 6,590 ⁺¹⁵⁰/₋₁₆₀ to 6,550 ⁺¹⁵⁰/₋₁₆₀ cal BP also points towards shallow water conditions as indicated by the micropaleontologically results (Fig. 6). Such shallow water conditions support bioproductivity (BiSi) increases in Unit A1 and A2 to its maximum at ~6,740 ⁺¹⁷⁰/₋₁₇₀ cal BP (Fig. 6). The elevation of the lake's floor rapidly increases from ~8 m b.s.l. at 8,440 ⁺²⁰⁰/₋₂₅₀ (base of the VOV16 record) to ~0.5 m a.s.l. at 6,420 ⁺¹³⁰/₋₁₄₀ cal BP (Unit A1 and A2; Fig. 6). Therefore, results of the Voëlvlei record underline a higher sea level compared to today until 6,420 ⁺¹³⁰/₋₁₄₀ cal BP and thus support a proposed 445 local/regional relative sea level maximum of about +3.8 m a.s.l. (~7,600 – 5,800 cal BP) (Cooper et al., 2018) which occurred at the southern Cape.



The micropaleontological associations of Units B and C (6,420 ⁺¹³⁰/₋₁₄₀ cal BP until today) are completely different from those of Unit A1 and A2 (Fig. 5, 6). Many samples are barren of microfossils and freshwater taxa dominate other samples. One single test of the foraminifer *Ammonia* sp. found in the lowermost part of unit B and C is the only brackish water taxon (Murray, 2006) and probably reworked from older sediments where this species is very abundant (Fig. 5, 6). Therefore, we assume freshwater or athalassic conditions for samples with aquatic taxa. New to Unit B and C are the freshwater ostracod species *Sarscypridopsis aculeata* and ehippia of cladocerans, which are typical of non-permanent water bodies (Frenzel, 2019; Meisch, 2000). They likely reflect the transformation of Voëlvlei to a non-permanent lake and terrestrial habitat. The lower part of Unit B contains variable amounts of plant remains and charcoal indicating river transport. Their later disappearance points to an isolation of the basin while silting up.

Decreasing elemental marine indicators (Na, Br/Zr-ratios) support reduced intrusion of marine waters from 6,420 ⁺¹³⁰/₋₁₄₀ cal BP (Fig. 6). Sedimentation rates markedly decrease while the occurrence of calcite (6,290 ⁺²⁴⁰/₋₁₅₀ - 4,590 ⁺⁵⁹⁰/₋₅₅₀ cal BP) further supports shallow water conditions in Units B and C (Fig. 6). While further silting up led to a location of the sediment surface above the present sea level (0 m a.s.l.) from 6,510 ⁺¹⁴⁰/₋₁₅₀ cal BP (Fig. 6) marine water intrusion was likely absent from 4,300 ⁺⁴⁹⁰/₋₅₇₀ cal BP when the sediment surface reached 3 m a.s.l. This is based on considering a still elevated sea level of about +1 m a.s.l. (5,300 – 4,200 cal BP) (Cooper et al., 2018) and a tidal range comparable to today (neap tide: 0.6 – 0.8 m, spring tide: 1.8 – 2 m) (Cooper, 2018, Rautenbach et al., 2019).

Overall, the results of this study only provide evidence of marine water intrusion in the Voëlvlei system rather than sea level index points and thus cannot be used to generate or corroborate an exact relative sea level curves (e.g., Compton, 2006; Cooper et al., 2018). However, in local/regional comparison the results of this study are in line with the findings from Eilandvlei (Kirsten et al., 2018b; Wündsche et al., 2018) and Groenvlei (Wündsche et al., 2016a) which indicate a rising sea level during the Early Holocene and a high-stand during the Mid Holocene. They therefore, support the assumed sea level evolution at the southern Cape coast of South Africa (Kirsten et al., 2018b; Marker and Miller, 1993; Reddering, 1988; Wündsche et al., 2018; Wündsche et al., 2016a). In (supra-)regional comparison, these results are also in line with studies from the west coast of South Africa (Baxter and Meadows, 1999; Carr et al., 2015; Kirsten et al., 2020) and Namibia (Compton, 2006), as reviewed in Cooper et al. (2018) showing a rapid sea level rise to a maximum of +3.8 m a.s.l. (~7,600 – 5,800 cal BP), followed by decrease to +1 m a.s.l. (5,300 – 4,200 cal BP) and a relatively constant sea level, comparable to the present, thereafter (Fig. 6).

[Figure 6]

475 5.3 Paleoenvironmental and –climate evolution

The main driver of the $\delta^2\text{H}_{n\text{-alkane}}$ signal at Voëlvlei is the $\delta^2\text{H}$ variability of the precipitation source (Strobel et al., 2020) although it has to be noted that variations in the vegetation composition, e.g., varying biosynthetic fractionation, evapotranspirative enrichment and water use efficiency possibly alter the $\delta^2\text{H}_{n\text{-alkane}}$ signal (Hou et al., 2007; Sachse et al., 2012). However, modern reference material from topsoils suggest that Westerly-derived precipitation is ^2H depleted and



480 Easterly-derived precipitation is ^2H enriched pointing to the ‘source effect’ as dominant driver of the $\delta^2\text{H}_{n\text{-alkane}}$ signal at Voëlvlei (Braun et al., 2017; Harris et al., 2010; Strobel et al., 2020; Table 1). $\delta^2\text{H}_{n\text{-alkane}}$ values from Voëlvlei are moderate from 8,440 $^{+200}/_{-250}$ to 7,070 $^{+160}/_{-200}$ cal BP, which imply a year-round precipitation regime, i.e., contributions of both Westerly- and Easterly-derived precipitation (Fig. 7a).

Year-round precipitation is accompanied by ^{13}C enriched $\delta^{13}\text{C}_{n\text{-alkane}}$ values between 8,440 $^{+200}/_{-250}$ and 7,070 $^{+160}/_{-200}$ cal BP, likely indicating overall dry conditions for this period at Voëlvlei (Fig. 7f). These dry conditions potentially led to a sparse
485 vegetation cover and runoff (induced by occasional events) which likely carries extremely variable grain sizes and amounts of allochthonous input (Al concentration, Al/Zr-ratios) (Fig. 7h). Minima in Al concentrations and Al/Zr-ratios are assumed to be caused by layers consisting nearly exclusively of sand (SiO_2) and thus also imply high allochthonous inputs (Fig. 2, 7h). Similarly at Vankervelsvlei, input of reworked soil material during this time is likely a result of low vegetation cover in the
490 catchment (Strobel et al., 2019). This interpretation of dry conditions between 8,440 $^{+200}/_{-250}$ and 7,070 $^{+160}/_{-200}$ cal BP is also in line with the findings from Eilandvlei, where low Afrotemperate forest (AFT) pollen percentages are interpreted as overall dry conditions between ~8,500 and 7,000 cal BP (Quick et al., 2018) (Fig. 7e) and a study at Seweweekspoort, where ^{15}N depleted $\delta^{15}\text{N}$ values are also interpreted to indicate moderately dry conditions (Chase et al., 2017) (Fig. 7c) resulting in a consistent moisture signal in the YRZ during this time.

495

[Figure 7]

At 7,020 $^{+170}/_{-200}$ cal BP, overall moister conditions are indicated by a distinct shift to ^{13}C depleted $\delta^{13}\text{C}_{n\text{-alkane}}$ values and high allochthonous input (Al content, Al/Zr-ratios), which lasts until present. Although, there is a decrease in allochthonous input
500 from 6,420 $^{+130}/_{-140}$ to 6,080 $^{+320}/_{-240}$ cal BP, and at 4,480 $^{+580}/_{-540}$ and 3,530 $^{+500}/_{-470}$ cal BP (Fig. 7h). The latter is accompanied by distinctly ^{13}C depleted $\delta^{13}\text{C}$ values (Fig. 7f) whereas the earlier one only shows slightly ^{13}C depleted values. This potentially indicates a denser vegetation cover, reducing runoff-induced sediment input, which is supported by the presence of freshwater taxa during this time (Fig. 5). However, drier conditions inferred from reduced allochthonous input could also be possible which might cause drought-induced changes of the vegetation composition, i.e., higher proportion of plants using CAM
505 metabolism. These could possibly reduce drought-stress and therefore the influence of water use efficiency to ^{13}C enrichment in the $\delta^{13}\text{C}_{n\text{-alkane}}$ values (Diefendorf and Freimuth, 2017). Therefore, the climatic deviations at 4,480 $^{+580}/_{-540}$ and 3,530 $^{+500}/_{-470}$ cal BP interrupting the trend towards moister conditions cannot be ultimately attributed to even moister or drier conditions. Noticeable are three data points at 6,670 $^{+170}/_{-170}$, 6,560 $^{+150}/_{-160}$ and 6,440 $^{+130}/_{-140}$ cal BP showing strongly ^{13}C enriched $\delta^{13}\text{C}_{n\text{-alkane}}$ values which exceed all other measurements and are accompanied by distinctly ^2H depleted $\delta^2\text{H}_{n\text{-alkane}}$
510 values (grey dots in Fig. 7a, e). For those three samples, the climate signal is possibly overprinted by local effects of plants that grow at shallower water depths and/or at the shoreline of the lake. While ^{13}C enriched $\delta^{13}\text{C}_{n\text{-alkane}}$ values point to the presence of plants using C4 and/or CAM metabolism (Boom et al., 2014; Carr et al., 2015; Diefendorf and Freimuth, 2017), the $\delta^2\text{H}_{n\text{-alkane}}$ signal with ^2H depleted values can be biased by the photosynthetic mode and also salinity (Aichner et al., 2017;



Feakins and Sessions, 2010; Ladd and Sachs, 2012; Sachse et al., 2012). Therefore, disentangling the regional climate and
515 local overprinting is challenging for the three aforementioned data-points. However, since allochthonous input is high (Al
concentration, Al/Zr-ratios; Fig. 7h), we hypothesize, overall moist conditions since 7,020 ⁺¹⁷⁰/₋₂₀₀ cal BP.

Moister conditions are accompanied by ²H depleted $\delta^2\text{H}_{n\text{-alkane}}$ values from 7,020 ⁺¹⁷⁰/₋₂₀₀ to 6,420 ⁺¹³⁰/₋₁₄₀ cal BP which are
likely indicative for a dominance of Westerly-derived precipitation (Fig. 7a). Contemporary to the aforementioned reduction
of the allochthonous input, there is also a marked shift to ²H enriched $\delta^2\text{H}_{n\text{-alkane}}$ values at 6,420 ⁺¹³⁰/₋₁₄₀ implying an increased
520 contribution of Easterly-derived precipitation (Fig. 7a). Afterwards, $\delta^2\text{H}_{n\text{-alkane}}$ values are variable, but have an overall trend to
²H depleted $\delta^2\text{H}_{n\text{-alkane}}$ values lasting until 2,060 ⁺¹⁴⁰/₋₂₀₀ cal BP which is likely indicative for a return to a dominance of
Westerly-derived precipitation (Fig. 7a). However, this period is interrupted by a short phase of somewhat ²H depleted values
from 5,560 ⁺⁴³⁰/₋₄₇₀ to 5,150 ⁺³⁴⁰/₋₃₃₀, indicating more Westerly-derived precipitation (Fig. 7a). From 2,060 ⁺¹⁴⁰/₋₂₀₀ cal BP until
present, ²H enriched $\delta^2\text{H}_{n\text{-alkane}}$ values imply an increased contribution of Easterly-derived precipitation (Fig. 7a), which occurs
525 within a trend towards moister conditions (¹³C depleted $\delta^{13}\text{C}_{n\text{-alkane}}$) (Fig. 7f).

Moist conditions between 7,000 and 4,700 cal BP are in line with studies from the central southern Cape coast (Quick et al.,
2018; Strobel et al., 2019; Wüdsch et al., 2018). However, beside increased moisture, also an increased wind driven
evapotranspiration was reconstructed at Vankervelsvlei (Strobel et al., 2019). The latter is also possibly related to an increased
Westerly wind belt and thus in line with the findings of this study showing intensified Westerly-derived precipitation at
530 Voëlvlei (Fig. 7d, e). At ~4,700 cal BP, climatic spikes were also detected in numerous studies located in the YRZ. In the
Wilderness area at the southern Cape coast, dry conditions but low wind-driven evapotranspiration were reconstructed during
this time (Quick et al., 2018; Strobel et al., 2019; Wüdsch et al., 2018) (Fig. 7d, e). After 4,700 cal BP, the overall trend in
increasing moisture availability at the central southern Cape coast is again in line with our findings at Voëlvlei (du Plessis et
al., 2020; Quick et al., 2018; Strobel et al., 2019; Wüdsch et al., 2018). $\delta^2\text{H}_{n\text{-alkane}}$ and $\delta^{13}\text{C}_{n\text{-alkane}}$ from marine sediments
535 recovered off the mouth of the Gouritz River (GeoB18308-2; Fig. 1) show a very similar pattern to Voëlvlei over the past
4,000 cal BP (Hahn et al., 2017) (Fig. 7). Those findings thus support our findings from Voëlvlei providing a consistent
regional picture for the southern Cape coast.

At Seweweekspoort, ~100 km inland, $\delta^{15}\text{N}$ values follow the pattern of $\delta^2\text{H}_{n\text{-alkane}}$ from Voëlvlei (Fig. 7c). There, climate is
thought to be dry from ~7,000 to ~4,700 cal BP and ~3,000 to ~1,000 cal BP due reduced Easterly-related precipitation (Chase
540 et al., 2017) (Fig. 7c). Climatic spikes to moister conditions at Seweweekspoort contradict the aforementioned results from the
wilderness area during this time, but are well reflected in spikes in the $\delta^2\text{H}_{n\text{-alkane}}$ record from Voëlvlei towards ²H enriched
 $\delta^2\text{H}_{n\text{-alkane}}$ values indicating increased Easterly-related precipitation contribution (Fig. 7a, c). In this context, previous studies
hypothesise that the non-dominant component of the temperate (Westerly)/tropical (Easterly) dynamic determines hydro-
climatic variability in southern Africa (e.g., Chase et al., 2017; Chase et al., 2015). More precisely, this means that although
545 Easterly (Westerly)-derived precipitation is relatively low in the western (eastern) parts of the YRZ, variability in the overall
moisture signal is thought to strongly depend on moisture contribution from this minor component (e.g., Chase et al., 2017;
Chase et al., 2015). The $\delta^2\text{H}_{n\text{-alkane}}$ values of this study imply increased Westerly-derived precipitation during drier phases at



Seweweekspoort and increased Easterly-derived precipitation during moister phases at Seweweekspoort (Fig. 7c), at a time generally characterised by a trend towards moister conditions at Voëlvlei (Fig. 7f). Moist conditions between 7,000 and 5,500 cal BP were also found in the north-south expanded Cape Fold Mountains at the western Cape (Chase et al., 2019 and references therein), indicating an overall moist period for south-western South Africa during this time which is perfectly in line with the increased Westerly precipitation contribution at Voëlvlei.

However, an opposite pattern is proposed to exist between sites located inland of the Cape Fold mountains (e.g., Seweweekspoort, Katbakkies Pass) and coastal sites from the southern Cape coast (e.g., Eilandvlei) (Chase and Quick, 2018; Quick et al., 2018). There are still discrepancies due to the comparison of different proxies in these studies compared to those from the southern Cape coast. Comparing our $\delta^2\text{H}_{n\text{-alkane}}$ -record from Voëlvlei, which is representative for fluctuations in the major moisture sources, with the $\delta^{15}\text{N}$ from Seweweekspoort (Chase et al., 2017), in detail many similarities are apparent confirming the assumption that hydrological variations at Seweweekspoort are driven by variations in Easterly-derived precipitation. In contrast, at the South Coast of South Africa including Voëlvlei the overall moisture evolution is not restricted to one moisture source and thus driven by a combination of both Westerly- and Easterly-derived precipitation.

The topmost sediments of Voëlvlei mainly consist of two fluvial flooding events (at $830^{+110}/_{-110}$ and $10^{+10}/_{-10}$ cal BP) which deposited large amounts of sediment (~15 cm and ~30 cm, respectively; Fig. 2; 7). Considering the dating error, the most recent flooding event is likely to be associated with the so called 'Laingsburg flood' from January 1981 (Damm and Hagedorn, 2010 and references therein). In marine sediments recovered off the mouth of the Gouritz River (GeoB18308-2; Fig. 1) major flooding events were detected between 650 and 300 cal BP and thus support our findings (Hahn et al., 2017).

Conclusions

Our multi-proxy record from lake Voëlvlei provides new insights in the sea level and paleoclimate history of the past 8.5 ka at the southern Cape Coast. Various dating approaches including OSL and ^{14}C of bulk TOC, organic macrofossils, charcoal and *n*-alkanes, were applied to the sediments to establish a robust chronology. Three temporal eco-zones can be characterised for Voëlvlei. These are related to sea level variations and are in line with the results of regional investigations in implying a subtidal marine-brackish followed by an intratidal brackish from $8,440^{+200}/_{-250}$ to $6,420^{+130}/_{-140}$ cal BP, and a freshwater to terrestrial system due to silting up of Voëlvlei, thereafter. In terms of climate, dry conditions accompanied by year-round precipitation contribution prevail from $8,440^{+200}/_{-250}$ to $7,070^{+160}/_{-200}$ cal BP followed by moister conditions and more Westerly-derived precipitation contributions from $7,070^{+160}/_{-200}$ to $6,420^{+130}/_{-140}$ cal BP followed by a distinct shift to an Easterly-dominance at 6,420 cal BP. An overall trend to a Westerly- lasting until 2,060 cal BP is followed by a trend towards an Easterlies-dominance, but both phases show several climatic spikes.

Our results are in good agreement with previous studies with regard to sea level changes on the western and southern coast of South Africa. The paleohydrological evolution of Voëlvlei is comparable to previous investigations from the Southern Cape coast during the past 8.5 ka, demonstrating an interplay of both Westerly- and Easterly-derived precipitation contribution. In



580 contrast, hydrological variations at Seweweekspoort, located within the interior of central southern South Africa, a region
hypothesised to show distinct hydroclimatic trends (relative to the coastal zones) through the Holocene, shows many
similarities to the Voëlvlei $\delta^2\text{H}_{n\text{-alkane}}$ record, indicating that moisture is driven by variations in Easterly-derived precipitation
there. Thus, the Voëlvlei $\delta^2\text{H}_{n\text{-alkane}}$ record provides valuable insights in the source of precipitation at the Southern Cape coast
during the past 8.5 ka.

585 Acknowledgements

This study was funded by the German Research Foundation (DFG) (HA 5089/11-1; ZE 860/6-1) and the German Federal
Ministry of Education and Research (BMBF) within the collaborative projects “Regional Archives for Integrated
Investigations” (RAiN) (grant no.: 03G0862B) and TRACES (Tracing Human and Climate impacts in South Africa) (grant
no.: 03F0798A) which are embedded in the international research programme SPACES (Science Partnership for the
590 Assessment of Complex Earth System Processes). PS gratefully acknowledges the support by a fellowship from the state of
Thuringia (Landesgraduiertenstipendium). Particularly acknowledged are C. Berndt, N. Blaubach, T. Eggert, C. Gregori, P.
Rauh, M. Steinich and M. Wagner for assistance in the lab. G. Daut is thanked for supporting the XRD measurements. N. du
Plessis, J. Baade, S. Hess, C. Gregori, R. Mäusbacher and M.E. Meadows are thanked for their fieldwork contributions and
constructive discussions. The participants of the 2019 course on Paleoenvironmental Analysis at Friedrich Schiller University
595 Jena supported us in micropaleontological sample preparation and picking of microfossils for an initial batch of subsamples.

References

- Aichner, B., Hilt, S., Périllon, C., Gillefalk, M., and Sachse, D.: Biosynthetic hydrogen isotopic fractionation factors during
lipid synthesis in submerged aquatic macrophytes: Effect of groundwater discharge and salinity, *Organic Geochemistry*,
113, 10-16, 2017.
- 600 Aitken, M. J.: *Thermoluminescence Dating*, Academic Press, London, 1985.
- Babel, M. and Schreiber, B.: *Geochemistry of Evaporites and Evolution of Seawater*. 2014.
- Barnes, R. S. K.: Little-known and phylogenetically obscure South African estuarine microgastropods (Mollusca:
Truncatelloidea) as living animals, *Journal of Natural History*, 52, 87-113, 2018.
- Baxter, A. J. and Meadows, M. E.: Evidence for Holocene sea level change at Verlorenvlei, Western Cape, South Africa,
605 *Quaternary International*, 56, 65-79, 1999.
- Bell, W. T.: Thermoluminescence dating: radiation dose rate data, *Archaeometry*, 21, 243-245, 1979.
- Benson, R. H. and Maddocks, R. F.: Recent ostracodes of Knysna Estuary, Cape Province, Union of South Africa, *The
University of Kansas Palaeontological Contributions* 5, 1964.



- Birch, G. F., du Plessis, A., and Willis, J. P.: Offshore and onland geological and geophysical investigation in the Wilderness
610 Lakes Region, Transactions of the Geological Society of South Africa, 81, 339-352, 1978.
- Blaauw, M. and Christen, J. A.: Flexible Paleoclimate Age-Depth Models Using an Autoregressive Gamma Process, Bayesian
Anal, 6, 457-474, 2011.
- Bliedtner, M., von Suchodoletz, H., Schäfer, I., Welte, C., Salazar, G., Szidat, S., Haas, M., Dubois, N., and Zech, R.: Age and
origin of leaf wax *n*-alkanes in fluvial sediment–paleosol sequences and implications for paleoenvironmental
615 reconstructions, Hydrol. Earth Syst. Sci., 24, 2105-2120, 2020.
- Bliedtner, M., Zech, R., Kühn, P., Schneider, B., Zielhofer, C., and von Suchodoletz, H.: The potential of leaf wax biomarkers
from fluvial soil-sediment sequences for paleovegetation reconstructions - Upper Alazani River, central southern Greater
Caucasus (Georgia), Quaternary Science Reviews, 196, 62-79, 2018.
- Boom, A., Carr, A. S., Chase, B. M., Grimes, H. L., and Meadows, M. E.: Leaf wax *n*-alkanes and $\delta^{13}\text{C}$ values of CAM plants
620 from arid southwest Africa, Organic Geochemistry, 67, 99-102, 2014.
- Bowen, G. J.: The Online Isotopes in Precipitation Calculator, version 3.1. URL: <http://www.waterisotopes.org>, 2018. 2018.
- Bowen, G. J., Wassenaar, L. I., and Hobson, K. A.: Global application of stable hydrogen and oxygen isotopes to wildlife
forensics, Oecologia, 143, 337-348, 2005.
- Branch, G. M., Griffiths, C. L., Branch, M. L., and Beckley, L. E.: Two oceans. A guide to the marine life of southern Africa,
625 Struik Nature, Cape Town, 2010.
- Braun, K., Bar-Matthews, M., Ayalon, A., Zilberman, T., and Matthews, A.: Rainfall isotopic variability at the intersection
between winter and summer rainfall regimes in coastal South Africa (Mossel Bay, Western Cape Province), South African
Journal of Geology, 120, 323-340, 2017.
- Braun, K., Bar-Matthews, M., Matthews, A., Ayalon, A., Cowling, R. M., Karkanias, P., Fisher, E. C., Dyez, K., Zilberman,
630 T., and Marean, C. W.: Late Pleistocene records of speleothem stable isotopic compositions from Pinnacle Point on the
South African south coast, Quaternary Research, 91, 265-288, 2018.
- Braun, K., Bar-Matthews, M., Matthews, A., Ayalon, A., Zilberman, T., Cowling, R. M., Fisher, E. C., Herries, A. I. R., Brink,
J. S., and Marean, C. W.: Comparison of climate and environment on the edge of the Palaeo-Agulhas Plain to the Little
Karoo (South Africa) in Marine Isotope Stages 5–3 as indicated by speleothems, Quaternary Science Reviews, 235,
635 105803, 2020.
- Buggle, B., Wiesenberg, G. L. B., and Glaser, B.: Is there a possibility to correct fossil *n*-alkane data for postsedimentary
alteration effects?, Applied Geochemistry, 25, 947-957, 2010.
- Burrow, C.: Calc_MinDose(): Apply the (un)logged minimum age model (MAM) after Galbraith et al. (1999) to a given De
Distribution. Function version 0.4.4. In Kreutzer, S., Burrow, C. Dietze, M., Fuchs, M.C., Schmidt, C., Fischer, M.,
640 Friedrich, J. 2019. Luminescence: Comprehensive Luminescence Dating Data Analysis R package version 0.9.3., 2019.
2019.



- Carr, A. S., Boom, A., Chase, B. M., Meadows, M. E., and Grimes, H. L.: Holocene sea level and environmental change on the west coast of South Africa: evidence from plant biomarkers, stable isotopes and pollen, *Journal of Paleolimnology*, 53, 415-432, 2015.
- 645 Carr, A. S., Boom, A., Grimes, H. L., Chase, B. M., Meadows, M. E., and Harris, A.: Leaf wax *n*-alkane distributions in arid zone South African flora: Environmental controls, chemotaxonomy and palaeoecological implications, *Organic Geochemistry*, 67, 72-84, 2014.
- Chase, B. M., Boom, A., Carr, A. S., Chevalier, M., Quick, L. J., Verboom, G. A., and Reimer, P. J.: Extreme hydroclimate response gradients within the western Cape Floristic region of South Africa since the Last Glacial Maximum, *Quaternary Science Reviews*, 219, 297-307, 2019.
- 650 Chase, B. M., Boom, A., Carr, A. S., Quick, L. J., and Reimer, P. J.: High-resolution record of Holocene climate change dynamics from southern Africa's temperate-tropical boundary, Baviaanskloof, South Africa, *Palaeogeography, Palaeoclimatology, Palaeoecology*, 539, 109518, 2020.
- Chase, B. M., Chevalier, M., Boom, A., and Carr, A. S.: The dynamic relationship between temperate and tropical circulation systems across South Africa since the last glacial maximum, *Quaternary Science Reviews*, 174, 54-62, 2017.
- 655 Chase, B. M., Faith, J. T., Mackay, A., Chevalier, M., Carr, A. S., Boom, A., Lim, S., and Reimer, P. J.: Climatic controls on Later Stone Age human adaptation in Africa's southern Cape, *Journal of Human Evolution*, 114, 35-44, 2018.
- Chase, B. M., Lim, S., Chevalier, M., Boom, A., Carr, A. S., Meadows, M. E., and Reimer, P. J.: Influence of tropical easterlies in southern Africa's winter rainfall zone during the Holocene, *Quaternary Science Reviews*, 107, 138-148, 2015.
- 660 Chase, B. M. and Meadows, M. E.: Late Quaternary dynamics of southern Africa's winter rainfall zone, *Earth-Science Reviews*, 84, 103-138, 2007.
- Chase, B. M. and Quick, L. J.: Influence of Agulhas forcing of Holocene climate change in South Africa's southern Cape, *Quaternary Research*, 90, 303-309, 2018.
- Compton, J. S.: The mid-Holocene sea-level highstand at Bogenfels Pan on the southwest coast of Namibia, *Quaternary Research*, 66, 303-310, 2006.
- 665 Cooper, J. A. G., Green, A. N., and Compton, J. S.: Sea-level change in southern Africa since the Last Glacial Maximum, *Quaternary Science Reviews*, 201, 303-318, 2018.
- Damm, B. and Hagedorn, J.: Holocene floodplain formation in the southern Cape region, South Africa, *Geomorphology*, 122, 213-222, 2010.
- 670 Diefendorf, A. F. and Freimuth, E. J.: Extracting the most from terrestrial plant-derived *n*-alkyl lipids and their carbon isotopes from the sedimentary record: A review, *Organic Geochemistry*, 103, 1-21, 2017.
- Douglas, P. M. J., Pagani, M., Eglinton, T. I., Brenner, M., Curtis, J. H., Breckenridge, A., and Johnston, K.: A long-term decrease in the persistence of soil carbon caused by ancient Maya land use, *Nature Geoscience*, 11, 645-649, 2018.



- 675 Douglas, P. M. J., Pagani, M., Eglinton, T. I., Brenner, M., Hodell, D. A., Curtis, J. H., Ma, K. F., and Breckenridge, A.: Pre-aged plant waxes in tropical lake sediments and their influence on the chronology of molecular paleoclimate proxy records, *Geochimica et Cosmochimica Acta*, 141, 346-364, 2014.
- du Plessis, N., Chase, B. M., Quick, L. J., Haberzettl, T., Kasper, T., and Meadows, M. E.: Vegetation and climate change during the Medieval Climate Anomaly and the Little Ice Age on the southern Cape coast of South Africa: Pollen evidence from Bo Langvlei, *The Holocene*, doi: 10.1177/0959683620950444, 2020. 1-12, 2020.
- 680 Duller, G. A. T.: Assessing the error on equivalent dose estimates derived from single aliquot regenerative dose measurements, *Ancient TL*, 25, 15-24, 2007.
- Duller, G. A. T.: Distinguishing quartz and feldspar in single grain luminescence measurements, *Radiation Measurements*, 37, 161-165, 2003.
- Duller, G. A. T.: Single-grain optical dating of Quaternary sediments: why aliquot size matters in luminescence dating, *Boreas*, 37, 589-612, 2008.
- 685 Eglinton, T. I. and Eglinton, G.: Molecular proxies for paleoclimatology, *Earth and Planetary Science Letters*, 275, 1-16, 2008.
- Engelbrecht, C. J. and Engelbrecht, F. A.: Shifts in Koppen-Geiger climate zones over southern Africa in relation to key global temperature goals, *Theoretical and Applied Climatology*, 123, 247-261, 2016.
- Engelbrecht, C. J. and Landman, W. A.: Interannual variability of seasonal rainfall over the Cape south coast of South Africa and synoptic type association, *Climate Dynamics*, 47, 295-313, 2016.
- 690 Engelbrecht, C. J., Landman, W. A., Engelbrecht, F. A., and Malherbe, J.: A synoptic decomposition of rainfall over the Cape south coast of South Africa, *Climate Dynamics*, 44, 2589-2607, 2015.
- Engelbrecht, F. A., Landman, W. A., Engelbrecht, C. J., Landman, S., Bopape, M. M., Roux, B., McGregor, J. L., and Thatcher, M.: Multi-scale climate modelling over Southern Africa using a variable-resolution global model, *Water Sa*, 37, 647-658, 2011.
- 695 Feakins, S. J. and Sessions, A. L.: Crassulacean acid metabolism influences D/H ratio of leaf wax in succulent plants, *Organic Geochemistry*, 41, 1269-1276, 2010.
- Fey, M.: *Soils of South Africa*, Cambridge University Press, Cambridge, 2010.
- Fick, S. E. and Hijmans, R. J.: WorldClim 2: new 1-km spatial resolution climate surfaces for global land areas, *Int J Climatol*, 37, 4302-4315, 2017.
- 700 Frenzel, P.: Fossils of the southern Baltic Sea as palaeoenvironmental indicators in multi-proxy studies, *Quaternary International*, 511, 6-21, 2019.
- Fürstenberg, S., Gründler, N., Meschner, S., and Frenzel, P.: Microfossils in surface sediments of brackish waters on the west coast of South Africa and their palaeoecological implications, *African Journal of Aquatic Science*, 42, 329-339, 2017.
- 705 Galbraith, R. F., Roberts, R. G., Laslett, G. M., H., Y., and Olley, J. M.: Optical dating of single and multiple grains of quartz from Jinmium rock shelter, northern Australia: part I, Experimental design and statistical models, *Archaeometry*, 41, 339-364, 1999.



- Gierga, M., Hajdas, I., van Raden, U. J., Gilli, A., Wacker, L., Sturm, M., Bernasconi, S. M., and Smittenberg, R. H.: Long-stored soil carbon released by prehistoric land use: Evidence from compound-specific radiocarbon analysis on Soppensee lake sediments, *Quaternary Science Reviews*, 144, 123-131, 2016.
- Guérin, G., Mercier, N., and Adamiec, G.: Dose-rate conversion factors: update, *Ancient TL*, 29, 5-8, 2011.
- Haas, M., Bliedtner, M., Borodynkin, I., Salazar, G., Szidat, S., Eglinton, T. I., and Zech, R.: Radiocarbon Dating of Leaf Waxes in the Loess-Paleosol Sequence Kurtak, Central Siberia, *Radiocarbon*, 59, 165-176, 2017.
- Haas, M., Kaltenrieder, P., Ladd, S. N., Welte, C., Strasser, M., Eglinton, T. I., and Dubois, N.: Land-use evolution in the catchment of Lake Murten, Switzerland, *Quaternary Science Reviews*, 230, 106154, 2020.
- Haberzettl, T., Baade, J., Compton, J., Daut, G., Dupont, L., Finch, J., Frenzel, P., Green, A., Hahn, A., Hebbeln, D., Helmschrot, J., Humphries, M., Kasper, T., Kirsten, K., Mäusbacher, R., Meadows, M., Meschner, S., Quick, L., Schefuß, E., Wüdsch, M., and Zabel, M.: Paleoenvironmental investigations using a combination of terrestrial and marine sediments from South Africa - The RAIN (Regional Archives for Integrated iNvestigations) approach, *Zentralblatt für Geologie und Paläontologie, Teil I*, 2014, 55-73, 2014.
- Haberzettl, T., Kirsten, K. L., Kasper, T., Franz, S., Reinwarth, B., Baade, J., Daut, G., Meadows, M. E., Su, Y., and Mäusbacher, R.: Using ²¹⁰Pb-data and paleomagnetic secular variations to date anthropogenic impact on a lake system in the Western Cape, South Africa, *Quaternary Geochronology*, 51, 53-63, 2019.
- Hahn, A., Schefuß, E., Andò, S., Cawthra, H. C., Frenzel, P., Kugel, M., Meschner, S., Mollenhauer, G., and Zabel, M.: Southern Hemisphere anticyclonic circulation drives oceanic and climatic conditions in late Holocene southernmost Africa, *Climate of the Past*, 13, 649-665, 2017.
- Harris, C., Burgers, C., Miller, J., and Rawoot, F.: O- and H-isotope record of Cape Town rainfall from 1996 to 2008, and its application to recharge studies of Table Mountain groundwater, South Africa, *South African Journal of Geology*, 113, 33-56, 2010.
- Heaton, T. J., Köhler, P., Butzin, M., Bard, E., Reimer, R. W., Austin, W. E. N., Bronk Ramsey, C., Grootes, P. M., Hughen, K. A., Kromer, B., Reimer, P. J., Adkins, J., Burke, A., Cook, M. S., Olsen, J., and Skinner, L. C.: Marine20 - the marine radiocarbon age calibration curve (0–55,000 cal BP), *Radiocarbon*, doi: 10.1017/RDC.2020.68, 2020. 1-42, 2020.
- Herrmann, N., Boom, A., Carr, A. S., Chase, B. M., West, A. G., Zabel, M., and Schefuß, E.: Hydrogen isotope fractionation of leaf wax *n*-alkanes in southern African soils, *Organic Geochemistry*, 109, 1-13, 2017.
- Hoefs, M. J. L., Rijpstra, W. I. C., and Sinninghe Damsté, J. S.: The influence of oxic degradation on the sedimentary biomarker record I: evidence from Madeira Abyssal Plain turbidites, *Geochimica et Cosmochimica Acta*, 66, 2719-2735, 2002.
- Hogg, A. G., Heaton, T. J., Hua, Q., Palmer, J. G., Turney, C. S. M., Southon, J., Bayliss, A., Blackwell, P. G., Boswijk, G., Bronk Ramsey, C., Pearson, C., Petchey, F., Reimer, P., Reimer, R., and Wacker, L.: SHCal20 Southern Hemisphere calibration, 0–55,000 years cal BP, *Radiocarbon*, doi: 10.1017/RDC.2020.59, 2020. 1-20, 2020.
- Hou, J., D'Andrea, W. J., MacDonald, D., and Huang, Y.: Evidence for water use efficiency as an important factor in determining the δ D values of tree leaf waxes, *Organic Geochemistry*, 38, 1251-1255, 2007.



- Johnson, M. R., Anhausser, C. R., and Thomas, R. J.: The geology of South Africa, Geological Society of South Africa, Johannesburg/Council for Geoscience, Pretoria, 2006.
- 745 Kirsten, K. L., Fell, J., Frenzel, P., Meschner, S., Kasper, T., Wündsich, M., Meadows, M., and Haberzettl, T.: The spatial heterogeneity of micro- and meio-organisms and their significance in understanding coastal system dynamics, *Estuarine, Coastal and Shelf Science*, 213, 98-107, 2018a.
- Kirsten, K. L., Haberzettl, T., Wündsich, M., Frenzel, P., Meschner, S., Smit, A. J., Quick, L. J., Mäusbacher, R., and Meadows, M. E.: A multiproxy study of the ocean-atmospheric forcing and the impact of sea-level changes on the southern Cape coast, South Africa during the Holocene, *Palaeogeography, Palaeoclimatology, Palaeoecology*, 496, 282-291, 2018b.
- 750 Kirsten, K. L., Kasper, T., Cawthra, H. C., Strobel, P., Quick, L. J., Meadows, M. E., and Haberzettl, T.: Holocene variability in climate and oceanic conditions in the winter rainfall zone of South Africa—inferred from a high resolution diatom record from Verlorenvlei, *Journal of Quaternary Science*, 35, 572-581, 2020.
- Ladd, S. N. and Sachs, J. P.: Inverse relationship between salinity and *n*-alkane δD values in the mangrove *Avicennia marina*, *Organic Geochemistry*, 48, 25-36, 2012.
- 755 Marker, M. E. and Miller, D. E.: A midHolocene high stand of the sea at Knysna, *South African Journal of Science*, 89, 100-102, 1993.
- Martens, K., Davies, B. R., Baxter, A. J., and Meadows, M. E.: A contribution to the taxonomy and ecology of the Ostracoda (Crustacea) from Verlorenvlei (Western Cape, South Africa), *African Zoology*, 31, 22-36, 1996.
- Martin, A. R. H.: Pollen Analysis of Groenvlei Lake Sediments Knysna (South Africa), *Review of Palaeobotany and*
760 *Palynology*, 7, 107-144, 1968.
- Martin, A. R. H.: The stratigraphy and history of Groenvlei, a South African coastal fen, *Australian Journal of Botany*, 7, 142-167, 1959.
- Meisch, C.: Crustacea: Ostracoda. In: *Süßwasserfauna von Mitteleuropa*, Schwoerbel, J. and Zwick, P. (Eds.), Spektrum Akademischer Verlag, Heidelberg, Berlin, 2000.
- 765 Mejdahl, V.: Thermoluminescence dating: Beta-dose attenuation in quartz grains, *Archaeometry*, 21, 61-72, 1979.
- Mucina, L. and Rutherford, M. C.: The vegetation of South Africa, Lesotho and Swaziland, SANBI, Pretoria, 2006.
- Murray, A. S. and Wintle, A. G.: Luminescence dating of quartz using an improved single-aliquot regenerative-dose protocol, *Radiation Measurements*, 32, 57-73, 2000.
- Murray, A. S. and Wintle, A. G.: The single aliquot regenerative dose protocol: potential for improvements in reliability,
770 *Radiation Measurements*, 37, 377-381, 2003.
- Murray, J. W.: *Ecology and applications of benthic foraminifera*, Cambridge University Press, Cambridge, 2006.
- Ohlendorf, C. and Sturm, M.: A modified method for biogenic silica determination, *Journal of Paleolimnology*, 39, 137-142, 2008.



- Olsen, J., Kjær, K. H., Funder, S., Larsen, N. K., and Ludikova, A.: High-Arctic climate conditions for the last 7000 years
775 inferred from multi-proxy analysis of the Bliss Lake record, North Greenland, *Journal of Quaternary Science*, 27, 318-327,
2012.
- Pecharsky, V. K. and Zavalij, P. Y.: *Fundamentals of Powder Diffraction and Structural Characterization of Materials*. 2009.
- Poynter, J.G., Farrimond, P., Robinson, N., Eglinton, G., 1989. Aeolian-Derived Higher Plant Lipids in the Marine
Sedimentary Record: Links with Palaeoclimate, in: Leinen, M., Sarnthein, M. (Eds.), *Paleoclimatology and*
780 *Paleometeorology: Modern and Past Patterns of Global Atmospheric Transport*. Springer Netherlands, Dordrecht, pp. 435-
462.
- Prescott, J. R. and Hutton, J. T.: Cosmic ray contributions to dose rates for luminescence and ESR dating: Large depths and
long-term time variations, *Radiation Measurements*, 23, 497-500, 1994.
- Quick, L. J., Chase, B. M., Wüdsch, M., Kirsten, K., Chevalier, M., Mäusbacher, R., Meadows, M., and Haberzettl, T.: A
785 high-resolution record of Holocene climate and vegetation dynamics from the southern Cape coast of South Africa: pollen
and microcharcoal evidence from Eilandvlei, *Journal of Quaternary Science*, 2018. 1-14, 2018.
- Quick, L. J., Meadows, M. E., Bateman, M. D., Kirsten, K. L., Mäusbacher, R., Haberzettl, T., and Chase, B. M.: Vegetation
and climate dynamics during the last glacial period in the fynbos-afrotemperate forest ecotone, southern Cape, South
Africa, *Quaternary International*, 404, Part B, 136-149, 2016.
- 790 Reddering, J. S. V.: Evidence for a middle Holocene transgression, Keurbooms estuary, South Africa, *Palaeoecology of Africa*
19, 79-86, 1988.
- Reinwarth, B., Franz, S., Baade, J., Haberzettl, T., Kasper, T., Daut, G., Helmschrot, J., Kirsten, K. L., Quick, L. J., Meadows,
M. E., and Mäusbacher, R.: A 700-Year Record on the Effects of Climate and Human Impact on the Southern Cape Coast
Inferred from Lake Sediments of Eilandvlei, Wilderness Embayment, South Africa, *Geografiska Annaler Series A -*
795 *Physical Geography*, 95, 345-360, 2013.
- Ruff, M., Fahrni, S., Gäggeler, H. W., Hajdas, I., Suter, M., Synal, H. A., Szidat, S., and Wacker, L.: On-line Radiocarbon
Measurements of Small Samples Using Elemental Analyzer and MICADAS Gas Ion Source, *Radiocarbon*, 52, 1645-1656,
2010.
- Sachse, D., Billault, I., Bowen, G. J., Chikaraishi, Y., Dawson, T. E., Feakins, S. J., Freeman, K. H., Magill, C. R., McInerney,
800 F. A., van der Meer, M. T. J., Polissar, P., Robins, R. J., Sachs, J. P., Schmidt, H. L., Sessions, A. L., White, J. W. C., West,
J. B., and Kahmen, A.: Molecular Paleohydrology: Interpreting the Hydrogen- Isotopic Composition of Lipid Biomarkers
from Photosynthesizing Organisms, *Annual Review of Earth and Planetary Sciences*, 40, 221-249, 2012.
- Salazar, G., Zhang, Y. L., Agrios, K., and Szidat, S.: Development of a method for fast and automatic radiocarbon measurement
of aerosol samples by online coupling of an elemental analyzer with a MICADAS AMS, *Nuclear Instruments and Methods*
805 *in Physics Research Section B: Beam Interactions with Materials and Atoms*, 361, 163-167, 2015.
- Schmitt-Sinns, J.: *Rezente benthische Foraminiferen im Bereich des Benguelastroms, Südwestafrika Verbreitungsmuster und
ihre steuernden Faktoren*, PhD thesis,, University of Bonn, Germany 2008. 2008.



- Scott, L. and Lee-Thorp, J. A.: Holocene climatic trends and rhythms in southern Africa. In: Past Climate Variability through Europe and Africa, Battarbee, R. W., Gasse, F., and Stickley, C. E. (Eds.), Springer, Dordrecht, 2004.
- 810 Sessions, A. L.: Factors controlling the deuterium contents of sedimentary hydrocarbons, *Organic Geochemistry*, 96, 43-64, 2016.
- Song, Y. and Müller, G.: Freshwater sediments: Sinks and sources of bromine, *Naturwissenschaften*, 80, 558-560, 1993.
- Strachan, K. L., Hill, T. R., Finch, J. M., Barnett, R. L., and Frenzel, P.: Distribution of Salt-Marsh Foraminifera in Two South African Estuaries and the Application as Sea-Level Indicators, *Journal of Coastal Research*, 33, 619-631, 2017.
- 815 Strobel, P., Haberzettl, T., Bliedtner, M., Struck, J., Glaser, B., Zech, M., and Zech, R.: The potential of $\delta^2\text{H}_{n\text{-alkanes}}$ and $\delta^{18}\text{O}_{\text{sugar}}$ for paleoclimate reconstruction – A regional calibration study for South Africa, *Science of The Total Environment*, 716, 137045, 2020.
- Strobel, P., Kasper, T., Frenzel, P., Schitteck, K., Quick, L. J., Meadows, M. E., Mäusbacher, R., and Haberzettl, T.: Late Quaternary palaeoenvironmental change in the year-round rainfall zone of South Africa derived from peat sediments from 820 Vankervelsvlei, *Quaternary Science Reviews*, 218, 200-214, 2019.
- Struck, J., Bliedtner, M., Strobel, P., Schumacher, J., Bazarradnaa, E., and Zech, R.: Leaf wax *n*-alkane patterns and compound-specific $\delta^{13}\text{C}$ of plants and topsoils from semi-arid and arid Mongolia, *Biogeosciences*, 17, 567-580, 2020.
- Stuiver, M., Reimer, P. J., and Reimer, R. W.: CALIB 8.2 [WWW program] at <http://calib.org> (Accessed: 2020-8-20). 2020.
- Szidat, S., Salazar, G. A., Vogel, E., Battaglia, M., Wacker, L., Synal, H.-A., and Türler, A.: 14C Analysis and Sample 825 Preparation at the New Bern Laboratory for the Analysis of Radiocarbon with AMS (LARA), *Radiocarbon*, 56, 561-566, 2014.
- Talma, A. S. and Vogel, J. C.: Late Quaternary paleotemperatures derived from a speleothem from Cango Caves, Cape Province, South Africa, *Quaternary Research*, 37, 203-213, 1992.
- Tyson, P. D. and Preston-Whyte, R. A.: *The Weather and Climate of Southern Africa*, Oxford University Press, Cape Town, 830 2000.
- Ullman, W. J.: The fate and accumulation of bromide during playa salt deposition: An example from Lake Frome, South Australia, *Geochimica et Cosmochimica Acta*, 59, 2175-2186, 1995.
- Walters, W. L. and Griffiths, C. L.: Patterns of distribution, abundance and shell utilization amongst hermit crabs, *Diogenes brevirostris*, *South African Journal of Zoology*, 22, 269-277, 1987.
- 835 Weldon, D. and Reason, C. J. C.: Variability of rainfall characteristics over the South Coast region of South Africa, *Theoretical and Applied Climatology*, 115, 177-185, 2014.
- Weltje, G. J. and Tjallingii, R.: Calibration of XRF core scanners for quantitative geochemical logging of sediment cores: Theory and application, *Earth and Planetary Science Letters*, 274, 423-438, 2008.
- Wintle, A. G. and Murray, A. S.: A review of quartz optically stimulated luminescence characteristics and their relevance in 840 single-aliquot regeneration dating protocols, *Radiation Measurements*, 41, 369-391, 2006.



- Wündsche, M., Haberzettl, T., Cawthra, H. C., Kirsten, K. L., Quick, L. J., Zabel, M., Frenzel, P., Hahn, A., Baade, J., Daut, G., Kasper, T., Meadows, M. E., and Mäusbacher, R.: Holocene environmental change along the southern Cape coast of South Africa – Insights from the Eilandvlei sediment record spanning the last 8.9 kyr, *Global and Planetary Change*, 163, 51-66, 2018.
- 845 Wündsche, M., Haberzettl, T., Kirsten, K. L., Kasper, T., Zabel, M., Dietze, E., Baade, J., Daut, G., Meschner, S., Meadows, M. E., and Mäusbacher, R.: Sea level and climate change at the southern Cape coast, South Africa, during the past 4.2 kyr, *Palaeogeography Palaeoclimatology Palaeoecology*, 446, 295-307, 2016a.
- Wündsche, M., Haberzettl, T., Meadows, M. E., Kirsten, K. L., Kasper, T., Baade, J., Daut, G., Stoner, J. S., and Mäusbacher, R.: The impact of changing reservoir effects on the C-14 chronology of a Holocene sediment record from South Africa, *Quaternary Geochronology*, 36, 148-160, 2016b.
- 850 Zech, M., Bugge, B., Leiber, K., Marković, S., Glaser, B., Hambach, U., Huwe, B., Stevens, T., Sümege, P., Wiesenberg, G., and Zöller, L.: Reconstructing Quaternary vegetation history in the Carpathian Basin, SE-Europe, using *n*-alkane biomarkers as molecular fossils, *E&G – Quaternary Science Journal*, 58, 2010.
- Zech, W., Schad, P., and Hintermaier-Erhard, G.: Böden der Welt Ein Bildatlas. In: EBL-Schweitzer, 2014.
- 855



Figures

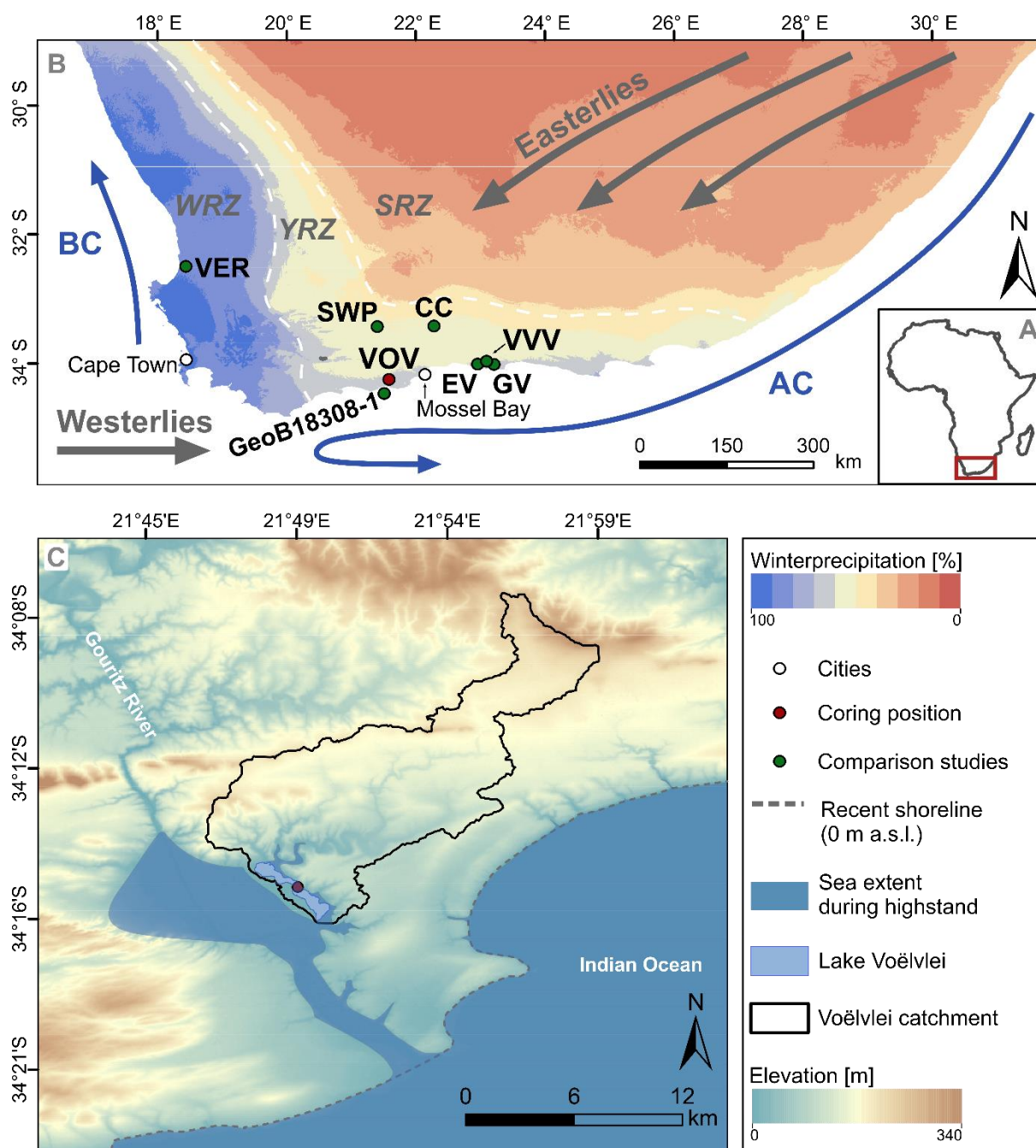
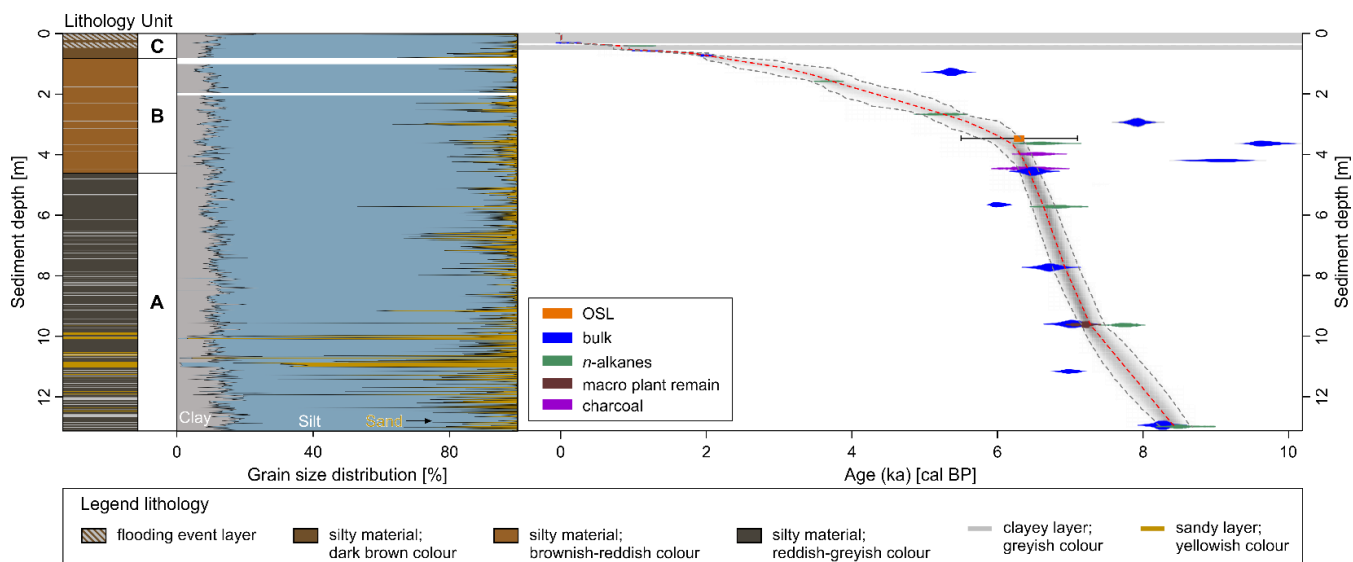
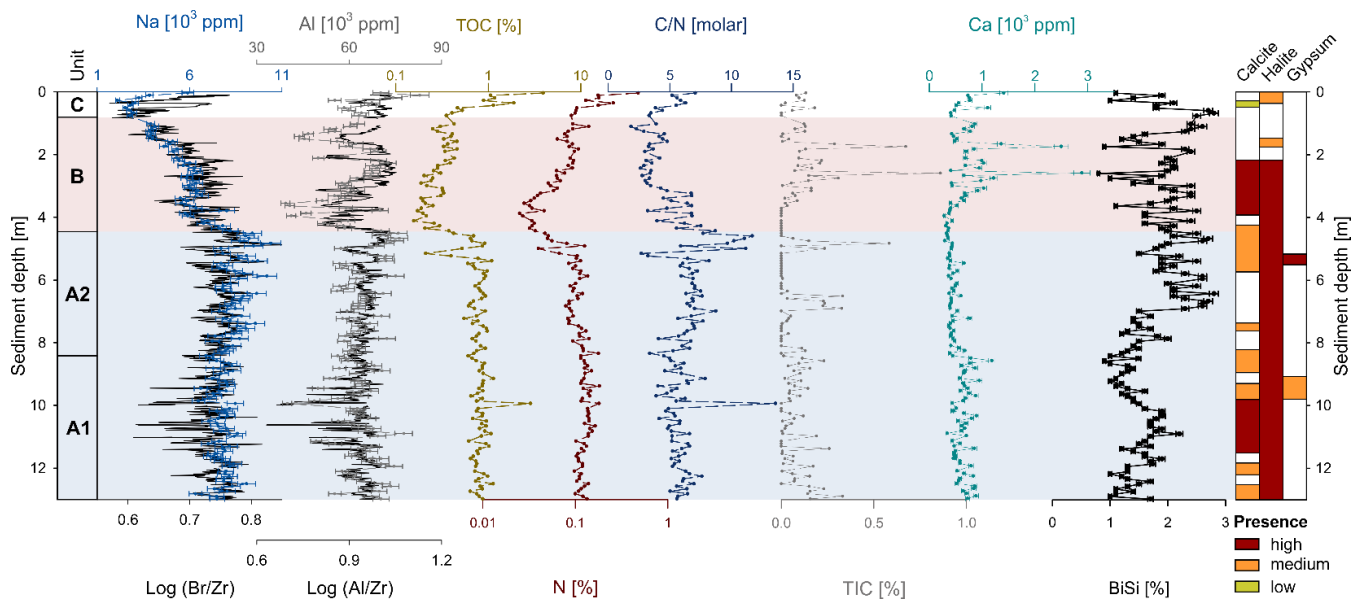


Figure 1: A) Simplified map of Africa. The red box highlights the studied area. B) Location of lake Voelvlei and studies mentioned in the text. Additionally, the circumpolar Westerlies, the tropical Easterlies, the Agulhas Current (AC) and the Benguela Current (BC) are depicted. C) Voelvlei, its catchment, the coring position as well as a paleo-sea level highstand (+5 m) and the recent shoreline (Data source: Rainfall seasonality: Worldclim 2 dataset (Fick and Hijmans, 2017); Circulation systems after Chase and Meadows (2007), DEM: SRTM 1 arc-second (~30 m)).

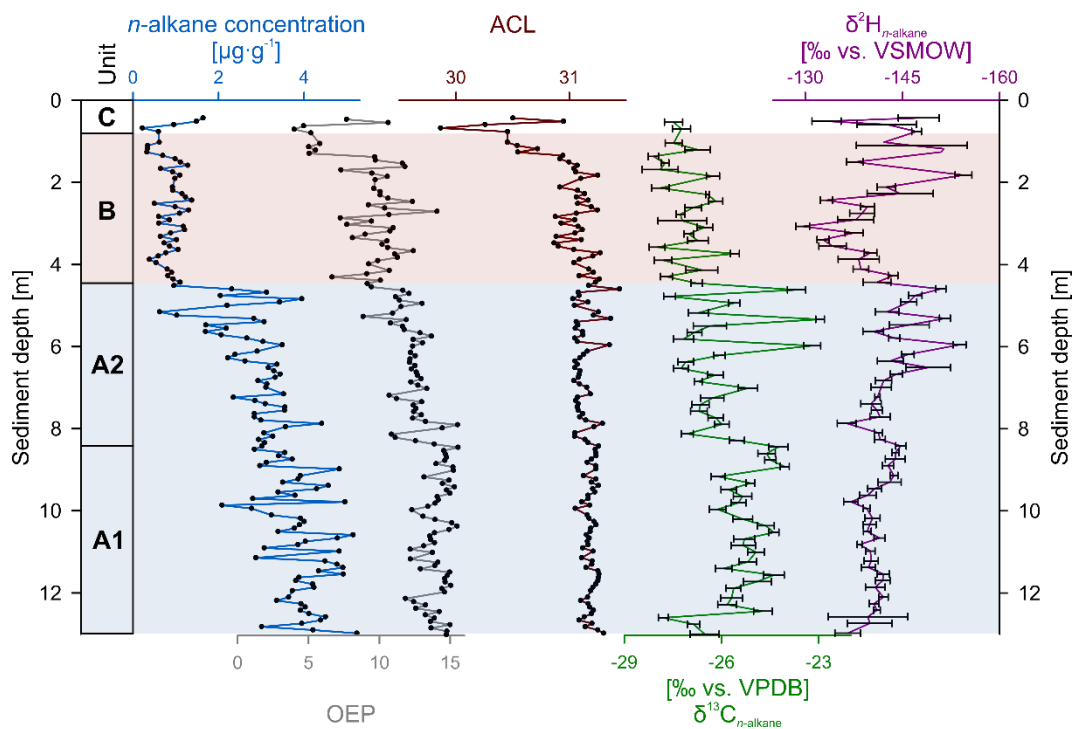
860



865 **Figure 2: left: Lithology and grain size distribution (clay, silt, sand) of the VOV16 record from Voëlvei. Right: Age-depth model of the sediment record from Voëlvei. Calibrated radiocarbon ages are displayed as probability density functions of the 2σ distributions (blue: bulk sediment; green: compound-class n-alkane samples; brown: macro plant remain). Calibration and age-depth modelling was carried out using the R software package Bacon 2.4.3 (Blauw and Christen, 2011). The logo of Copernicus Publications.**



870 **Figure 3: Lithological units, Sodium (Na) content and Log_{10} ratio of Bromine (Br) and Zirconium (Zr), Aluminium (Al) and Log_{10} ratio of Al and Zr, contents of Total Organic Carbon (TOC), total Nitrogen (N), molar C/N-ratio, Total Inorganic Carbon (TIC), Calcium (Ca) and Biogenic Silica (BiSi) derived from the sediment core VOV16 from Voëlvelei. The presence of selected mineral components is also depicted.**



875 **Figure 4:** Concentration, odd-over-even predominance (OEP) and average chain length (ACL) of leaf wax *n*-alkanes and their stable isotopic composition for hydrogen ($\delta^2\text{H}_{n\text{-alkane}}$) and carbon ($\delta^{13}\text{C}_{n\text{-alkane}}$) of the Voelvlei sediment record.

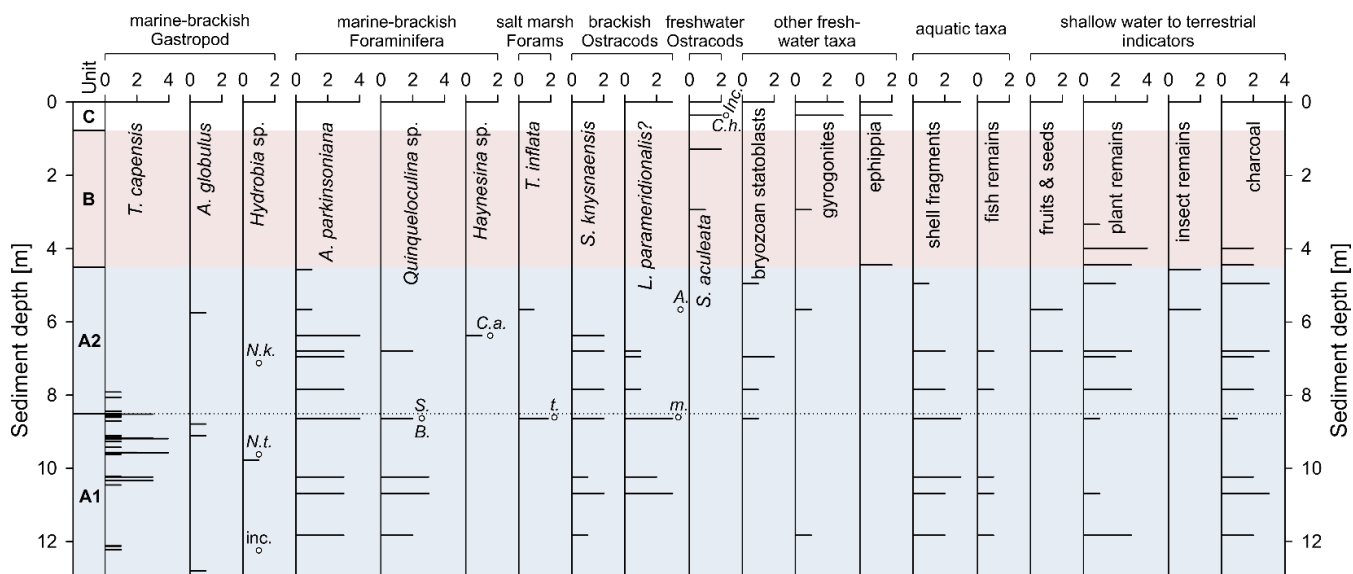
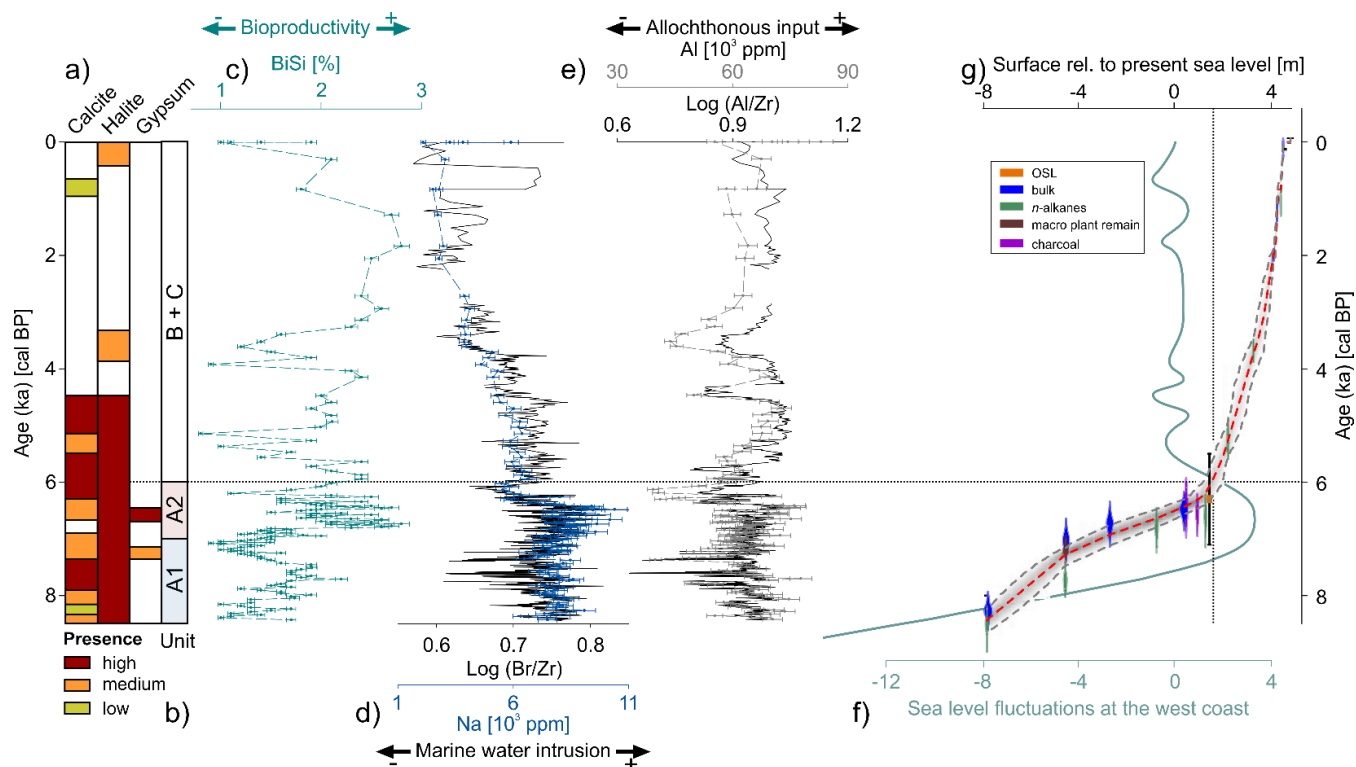


Figure 5: Distribution of micropaleontological taxa and charcoal in core VOV16. Units are based on distribution of micropaleontological taxa and lithological characteristics. Additional macrofossils were picked from the lowest part of the core where they are relatively abundant. All abundances are given semi-quantitatively (0 – absent, 1 – rare, 2 – common, 3 – abundant, 4 – very abundant). Single occurrences of taxa are indicated by empty circles and abbreviated name (Nassarius kraussianus, Natica tecta, Bolivina sp., Spirillina sp., Cribroelphidium articulatum, trochamminid foraminifer, Aglaiella, myodocopid ostracod, Cyprilla humilis).

880



885 **Figure 6:** a) Occurrence of selected mineral components in the VOV16 sediment record, b) lithological and paleoecological units (A1 – subtidal marine-brackish, A2 – intratidal brackish, B+C freshwater to terrestrial), c) Biogenic Silica (BiSi) content, d) Na content and Log (Br/Zr)-ratios, e) Al content and Log (Al/Zr)-ratios from Voëlvlei. f) Sea level curve for the west coast of South Africa (Compton, 2006; Cooper et al., 2018) and g) the lake floor of Voëlvlei relative to the present sea level.

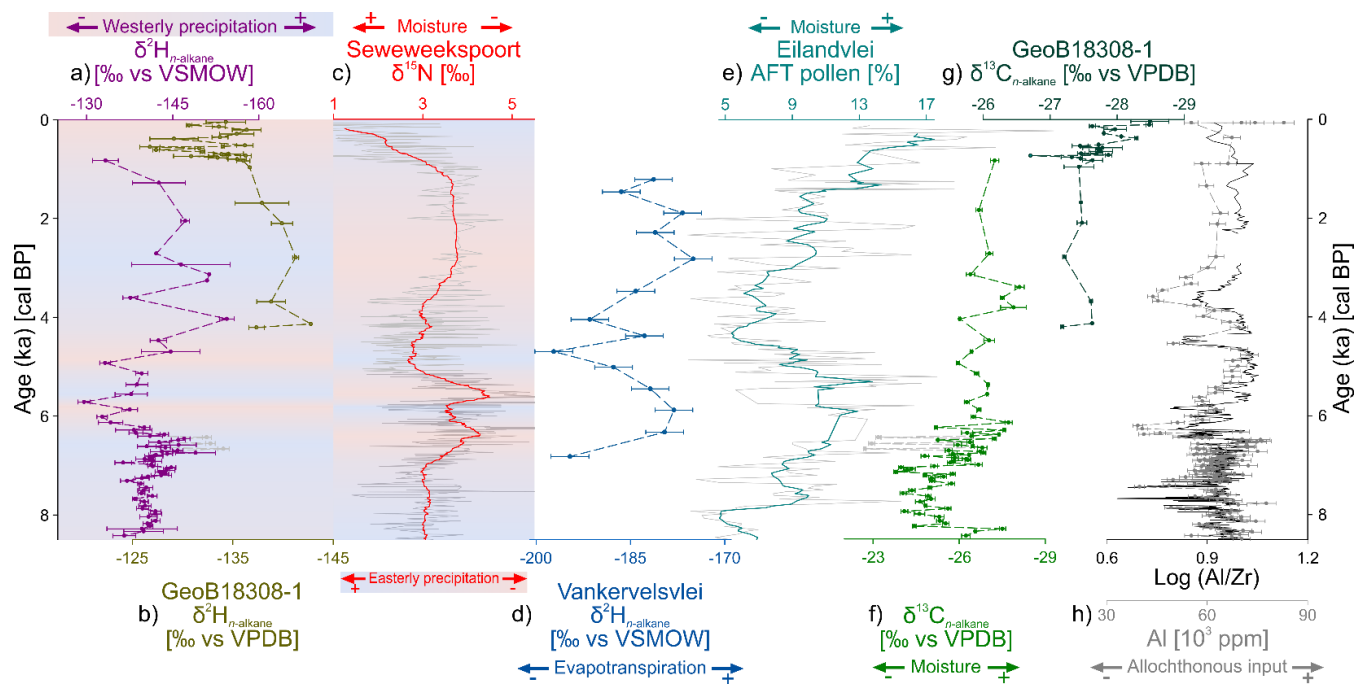


Figure 7: a) $\delta^2\text{H}_{n\text{-alkane}}$ from Voëlvlei compared to b) $\delta^2\text{H}_{n\text{-alkane}}$ from GeoB18308-1 (Hahn et al., 2017), c) $\delta^{15}\text{N}$ from Seweweekspoort (Chase et al., 2017), d) $\delta^2\text{H}_{n\text{-alkane}}$ from Vankervelsvlei (Strobel et al., 2019), e) Afrotemperate forest pollen (AFT) from Eilandvlei (Quick et al., 2018), f) $\delta^{13}\text{C}_{n\text{-alkane}}$ from Voëlvlei, g) $\delta^{13}\text{C}_{n\text{-alkane}}$ from GeoB18308-1 (Hahn et al., 2017), and h) Aluminium (Al) content and Log Al/Zr-ratio from Voëlvlei. The locations of the studies are depicted in Figure 1.

890



Tables

895 **Table 1: Modelled isotopic hydrogen composition of precipitation at Voëlvlei (Lat: 34.013° S; Lon: 22.904° E; Elevation: 5 m) (Bowen, 2018; Bowen et al., 2005).**

	Jan	Feb	Mar	Apr	May	Jun	Jul	Aug	Sep	Oct	Nov	Dec
$\delta^2\text{H}_p$ [‰ vs. V-SMOW]	6	4	3	-12	-21	-26	-29	-33	-23	-16	-12	-4



900

Table 2: Conventional radiocarbon ages as well as 2σ calibrated age ranges and median calibrated ages (Calib 8.2) (Stuiver et al., 2020) using the SHCal20 and Marine20 calibration curve (Heaton et al., 2020; Hogg et al., 2020) of dated bulk sediment, n-alkanes and organic macro particle (OMP) samples from the VOV16 record. Samples from the marine and brackish parts of the record were reservoir corrected using a ΔR of 134 ± 38 ¹⁴C yrs after Wündsche et al. (2016b). Too old and too young samples are highlighted by * and #, respectively.

Sediment depth [m]	Lab ID	1σ conventional ¹⁴ C age [BP]	Dated material	Median cal age and 2σ error [cal BP]	Calibration
0.29	Poz-94013	660 ± 30	bulk	610 ⁺⁷⁵ / ₋₂₅	1
0.32	BE-9770.1.1	-85 ± 120	bulk	100 ⁺⁸⁵ / ₋₈₅	1
0.44	BE-12027.1.1	1,250 ± 140	n-alkanes	1,110 ⁺²⁵⁰ / ₋₁₃₀	1
0.51	BE-9772.1.1	1,855 ± 120	bulk	1,740 ⁺²⁷⁰ / ₋₂₇₀	1
0.59	BE-9772.1.1	1,360 ± 120	bulk	1,210 ⁺⁴⁷⁰ / ₋₂₅₀	1
0.75	Poz-96323	2,080 ± 35	bulk	2,000 ⁺¹⁷⁰ / ₋₈₀	1
1.29	Poz-94014	5,330 ± 50	bulk	5,370 ⁺⁴¹⁰ / ₋₂₁₀	2 *
1.59	BE-12026.1.1	3,470 ± 90	n-alkanes	3,690 ⁺⁴⁵⁵ / ₋₂₄₀	1
2.68	BE-12025.1.1	4,630 ± 100	n-alkanes	5,280 ⁺⁵²⁰ / ₋₃₁₀	1
2.95	Poz-96324	7,780 ± 50	bulk	7,920 ⁺³⁸⁰ / ₋₁₉₀	2 *
3.64	BE-12024.1.1	5,830 ± 130	n-alkanes	6,600 ⁺⁵⁹⁰ / ₋₂₉₀	1
3.65	Poz-94016	9,250 ± 80	bulk	9,660 ⁺⁵⁵⁰ / ₋₂₅₀	2 *
3.99	BE-13598.1.1	5,780 ± 120	charcoal	6,550 ⁺⁵⁰⁰ / ₋₂₅₀	1
4.21	Poz-98909	8,750 ± 170	bulk	9,060 ⁺⁹⁰⁰ / ₋₄₈₀	2 *
4.57	Poz-98910	6,380 ± 40	bulk	6,490 ⁺³⁷⁰ / ₋₁₉₀	2
4.57	BE-13597.1.1	5,550 ± 110	charcoal	6,310 ⁺⁴⁵⁰ / ₋₂₁₀	1
4.57	BE-13596.1.1	5,800 ± 120	charcoal	6,570 ⁺⁵⁰⁰ / ₋₂₇₀	1
5.66	Poz-94017	5,740 ± 40	bulk	5,800 ⁺³⁷⁰ / ₋₂₀₀	2 #
5.73	BE-12023.1.1	6,020 ± 100	n-alkanes	6,830 ⁺⁴⁷⁰ / ₋₂₃₀	1
7.74	Poz-94018	6,590 ± 50	bulk	6,720 ⁺⁴²⁰ / ₋₂₁₀	2
9.61	Poz-94021	6,850 ± 50	bulk	7,020 ⁺⁴¹⁰ / ₋₂₁₀	2
9.63	Poz-94020	6,310 ± 50	OMP	7,200 ⁺¹⁶⁰ / ₋₅₀	1
9.64	BE-12022.1.1	6,940 ± 110	n-alkanes	7,750 ⁺³⁷⁰ / ₋₁₈₀	1
11.19	Poz-94022	6,620 ± 50	bulk	6,760 ⁺⁴²⁰ / ₋₂₁₀	2 #
12.95	Poz-94023	8,110 ± 50	bulk	8,270 ⁺³⁷⁰ / ₋₂₁₀	2
12.99	BE-12021.1.1	7,750 ± 110	n-alkanes	8,510 ⁺⁴⁶⁰ / ₋₁₉₀	1

1 SHCal20, 2 Marine20 and reservoir corrected using a ΔR of 134 ± 38 ¹⁴C yrs after Wündsche et al. (2016b)

905



Table 3: Equivalent dose measurements on sample VOV16-1. 24 aliquots were measured (a 25th with a De of ~125 Gy was excluded prior to analysis).

Average sediment depth [m]	Dose rate (Gy ka ⁻¹)	CAM D _e (Gy)	CAM OD [%]	MAM De (Gy)	CAM age (ka)	MAM age (ka)
3.50	3.01 ± 0.12	31.0 ± 2.8	40 ± 6	20.3 ± 2.3	10.3 ± 1.0	6.8 ± 0.8